SOL-GEL SYNTHESIS OF CORE-SHELL METAL OXIDE NANOPARTICLES AND THEIR APPLICATION IN NIR REFLECTIVE COATINGS

by

Sirada Janjaochay

A Thesis Submitted in Partial Fulfillment of the Requirements for the Degree of Master of Engineering in Nanotechnology

Examination Committee:	Dr. Tanujjal Bora (Chairperson)
	Dr. Sitthisuntorn Supothina (Co-Chairperson)
	Dr. Raffaele Ricco
	Prof. P. Abdul Salam
Nationality:	Thai
Previous Degree:	Bachelor of Engineering in Nano-Engineering
	Chulalongkorn University
	Bangkok, Thailand
Scholarship Donor:	Royal Thai Government Fellowship

Asian Institute of Technology
School of Engineering and Technology
Thailand
July 2022

AUTHOR'S DECLARATION

I, Sirada Janjaochay, declare that the research work carried out for this thesis was in accordance with the regulations of the Asian Institute of Technology. The work presented in it are my own and has been generated by me as the result of my own original research, and if external sources were used, such sources have been cited. It is original and has not been submitted to any other institution to obtain another degree or qualification. This is a true copy of the thesis, including final revisions.

Date: 15 July 2022

Name (in printed letters): SIRADA JANJAOCHAY

Signature: Sirada Janjaochay

ACKNOWLEDGMENTS

I would like to express my deepest appreciation to my advisor and co-advisor for their invaluable patience, support, and feedback. I am also deeply indebted to my defense committee, who generously shared their expertise and knowledge. Moreover, I could not have undertaken this journey without the Royal Thai Government fellowship and NSTDA-AIT top-up scholarship that financed my research.

I would like to extend my sincere thanks to laboratory assistants and characterization technicians from AIT and MTEC. I could not have done my lab work and characterization without their help. I am also grateful to my Nano members who shared their experience and energy with me.

Lastly, I would like to mention my family, especially my parents, for their support. Their motivation kept me active during the process. I would also like to thank my friends for all the emotional support.

ABSTRACT

With the increasing human population, the number of human-made architectures increases along with the people. The architectures release heat slower than natural infrastructures and destroy the heat cycle leading to the collected heat, especially in the city. This occurrence is called the urban heat island effect. Along with many solutions of city design, green infrastructures, and policies, the near-infrared (NIR) reflective structures are promising solutions to the issue. Coating with NIR reflective pigments, human-made architectures can obtain the cooling effect where the absorbed heat is decreased. TiO_2 is one of the most popular materials that provide high NIR reflectance to the pigments. This work reports core-shell nanostructures of metal oxides-TiO_2 since the core-shell structures prevent the nanoparticles' agglomeration and enhance the pigments' NIR reflectivity. The possible metal oxides cores are Cr_2O_3, Al_2O_3, and Fe_2O_3 nanoparticles, which are commercially available. In addition, sol-gel synthesis of the NIR reflective pigments is a simple, low-cost, and environmentally friendly approach. The possible factors that affect the NIR reflectance of the nanoparticles are investigated, such as the thickness of the TiO_2 shell, nanoparticle sizes, and fabrication conditions. The synthesized nanoparticles are then be analyzed with characterization tools, such as transmission electron microscopy, UV-vis-NIR spectrophotometer, etc., to study the properties and the cooling effect obtained from the coating of these pigments.

Keywords: TiO_2, Core-shell, Sol-gel synthesis, NIR reflection, Cool pigment

CONTENTS

LIST OF TABLES

LIST OF FIGURES

Page

Page

Page

LIST OF ABBREVIATIONS

ASA = Acrylonitrile-Styrene-Acrylate
ASTM = American Society for Testing and Materials
CIE = International Commission on Illumination
DI = Deionized
DNA = Deoxyribonucleic Acid
DSC = Differential Scanning Calorimetry
EDX = Energy Dispersive X-Ray
FESEM = Field Emissive Scanning Electron Microscope/ Microscopy
FTIR = Fourier Transform Infrared Spectroscopy
GHGs = Greenhouse Gases
HDPE = High Density Polyethylene
HVAC = Heating, Ventilation, and Air Conditioning
IR = Infrared
LDPE = Low Density Polyethylene
NIR = Near-Infrared
PS = Polystyrene
QUV = Q-panel Laboratory Ultraviolet testing
RT = Room Temperature
TBT = Tetrabutyl Orthotitanate/ Tetrabutyl Titanate/ Titanium (IV) Butoxide
TEM = Transmission Electron Microscope
TEOS = Tetraethyl Orthosilicate
TGA = Thermogravimetric Analysis
TSR = Total Solar Reflectance
TTIP = Titanium tetraisopropoxide/ Titanium Isopropoxide/ Titanium (IV) Isopropoxide
SEM = Scanning Electron Microscope/ Microscopy
UV = Ultraviolet
VBDs = Vector-Borne Diseases
XPS = X-ray Photoelectron Spectroscopy
XRD = X-Ray Diffraction

CHAPTER 1
INTRODUCTION

1.1 Background of the Study

Sunlight that reaches the Earth's surface can be categorized into three main regions, namely ultraviolet (UV) light, visible light, and infrared (IR) light. IR is a part of the solar spectrum with wavelengths ranging between 700nm to 2500 nm, constituting about 45% of the sunlight. The 700-1100 nm region is the heat-producing region known as near-infrared (NIR) and it is the largest portion of sunlight (Rosati et al., 2021). The absorption of NIR radiation causes a rise in the surface temperature (Fang et al., 2013; Malshe & Bendiganavale, 2008).

In the daytime, the natural surfaces absorb heat and re-emitted back to the atmosphere, which results in a natural heating-cooling cycle throughout the day. With the increase in human population, more natural areas are consumed and changed into cities with increasing concrete infrastructures, such as buildings, roads, and other infrastructures. Surfaces like concrete and asphalt (used in the roads) generally absorb more heat during the daytime due to their higher heat absorptivity than natural landscapes and also cool down slowly at night. The overall effect is a gradual increase in surrounding temperature in urban areas compared to the outlying areas, known as the '*heat island effect*', as shown in **Figure 1.1**, (Gago et al., 2013; Yang et al., 2016). The heat island effect increases the expenditure and energy consumption for interior cooling. Around 84% of the cooling energy comes from the burning of fossil fuels which releases an enormous amount of greenhouse gases (GHGs) and leads to global warming and climate change issues that directly impact human health and well-being, economic growth, and the environment (Ritchie & Roser, 2017).

Figure 1.1

The Figure Indicates the Higher Temperature in the Urban Than its Surrounding From the Heat Island Effect

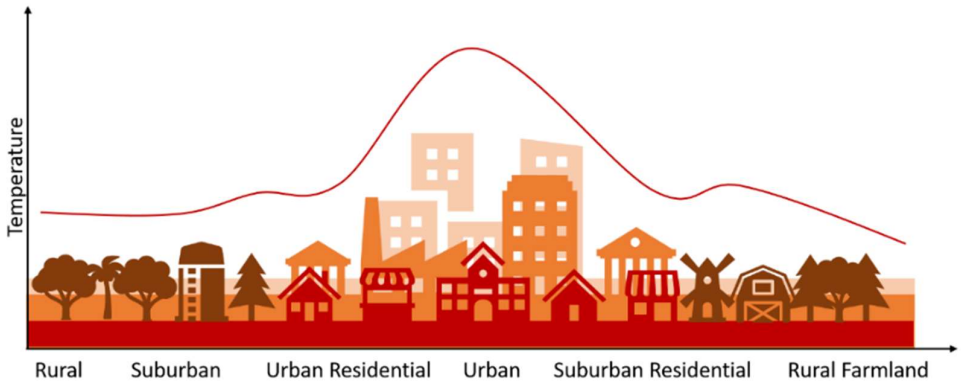

According to the US Environmental Protection Agency (EPA; www.epa.gov), trees, green roofs, and vegetation can help reduce urban heat island effects by shading building surfaces, deflecting the radiation from the sun, and releasing moisture into the atmosphere. Planting more trees and other vegetation is a nature-based solution to deal with the heat island effect. However, generally, cities provide less space for such green infrastructures. Therefore, the application of artificial green infrastructures, such as green roofs and green pavements, are encouraged these days as an alternative heat island reduction strategy, providing both direct and ambient cooling effects. In addition, green roofs improve air quality by reducing the heat island effect and absorbing pollutants (Manso et al., 2021; Shafique et al., 2018).

1.2 Statement of the Problem

Among the several countermeasures to deal with the heat island effect, the application of NIR reflective coatings is common, which provides high effectiveness, is low-cost, and can be applied by all sectors of society (Phelan et al., 2015). However, traditional NIR reflective materials, such as carcinogenic chromium and cobalt, are toxic to humans and the environment (Rosati et al., 2021). In addition, the durability of these coatings has to be further developed for long-term use and less cost of reparation from photooxidation and weathering.

TiO_2 is a material with high NIR reflectivity and has been used for NIR reflection applications. However, it can provide only white color which is not favorable for cool-coating on earth tones buildings and rooftops or other colorful surfaces. Mixing TiO_2 with other suitable materials of different colors can be an alternative. However, simple mixing of materials with TiO_2 particles is found to be less effective in terms of their stability and color tones. In this regard, the core-shell structure with TiO_2 as the shell layer has attracted recent attention as the structure can provide both the colors from its cores and NIR reflectivity from the TiO_2 shell (He et al., 2017; Sharma et al., 2018). In addition, the core-shell structure increases light scattering from the different refractive indexes of the core and shell materials (Rennel & Rigdahl, 1994). The TiO_2 shell also helps protect cores from reacting with other environmental factors, slowing down their degradation, and capturing the toxicity of the cores, if any (Soranakom et al., 2021).

Several methods have been explored to date to synthesize core-shell nanoparticles employing both top-down approaches, such as chemical etching, sputtering, laser ablation, etc., as well as bottom-up approaches, such as sol-gel synthesis, vapor deposition, aerogel methods, etc. (Shah et al., 2021) However, the top-down methods generally lack control over maintaining the particle shapes and sizes which greatly affects the optical properties of the particles. Often, they are also not suitable for large area applications and some techniques even require sophisticated environments, like a vacuum atmosphere, adding to the operating cost of the method. Bottom-up approaches in contrast have better control over maintaining the particle's shape and sizes and most of the bottom-up approaches are tunable proving the flexibility to play with the particle's chemistry to modulate their optical properties according to the user requirements. Especially sol-gel synthesis method for NIR reflective core-shell particles is of great interest due to its simplicity and low operating cost. The technique can be applied affordably to produce durable and non-toxic core-shell particles that can be applied for various applications. However, its application for developing NIR reflective particles is limited (Rosati et al., 2021), and needs further investigations to produce NIR reflective core-shell particles with different core materials for different color tones.

1.3 Objectives of the Study

The overall objective of this thesis is to synthesize core-shell metal oxide nanoparticles with high NIR reflection using a sol-gel technique. Reflecting NIR radiations is crucial in many applications where less heat absorption by a surface is desirable. The specific objectives of the research work are given below:

1. To synthesize core-shell metal oxide NIR reflecting nanoparticles using sol-gel technique. Here, titanium dioxide (TiO_2) will be used as the NIR reflecting component, which will form the shell layer on a core metal oxide nanoparticle, such as aluminum oxide (Al_2O_3), chromium oxide (Cr_2O_3), and iron oxide (Fe_2O_3). The core metal oxide will provide different colors to the pigment.
2. To study the NIR reflectance of the individual and mixed core-shell nanoparticles to obtain the highest NIR reflectance in the wavelength ranging up to 2500 nm.
3. To develop a NIR reflecting pigment using the core-shell nanoparticles and apply it on a surface to investigate the cooling effect of the pigment.

1.4 Scope of the Study

The scope of this research is within the field of NIR reflective pigments, where the study focuses on the application of metal oxide-based core-shell nanoparticles to develop the NIR reflective pigments. Sol-gel technique is explored for the synthesis of the core-shell nanoparticles. For the core, the study uses aluminum oxide (Al_2O_3), chromium oxide (Cr_2O_3), and iron oxide (Fe_2O_3) particles, while for the shell layer, titanium dioxide (TiO_2) is used. The study is primarily focused on the laboratory-scale prototype development for these NIR reflective pigments, and no real-time field experiments are conducted during the study.

1.5 Organization of the Study

This report contains five chapters as indicated as follows:

Chapter 1 is the background of the study, statement of the problem, objectives, scopes, and the organization of the study.

Chapter 2 is the literature review of the heat island effect's impacts on human health and well-being, economy, and environment; the countermeasures of the heat island effect; the fabrication routes of NIR reflective pigments; the sol-gel synthesis of Al_2O_3-

TiO_2, Fe_2O_3-TiO_2, and Cr_2O_3-TiO_2; and the cooling effect evaluation for the NIR reflective pigments.

Chapter 3 provides the methodology for the synthesis of the NIR reflective pigments; characterizations of the pigments; investigation of NIR reflectance; and the cooling effect evaluation.

Chapter 4 presents the results of the SEM, TEM, XRD, and particle size analysis characterizations, NIR reflectance evaluation of powder and coating samples, and cooling effect evaluation of the pigments.

Chapter 5 summarizes the thesis with a conclusion and future recommendations for this study.

CHAPTER 2
LITERATURE REVIEW

The heat island effect highly contributes to climate change and global warming issues where the severity is dramatically increased along with the population growth. There are several approaches to mitigate and reduce the impacts of the heat island effect, including technological responses and policy (Degirmenci et al., 2021). Technological responses are adaptive and promising countermeasures that can be further developed for higher effectiveness.

NIR reflective pigments are one of the technological responses that can provide a cooling effect to human-made infrastructures such that the heat island effect issue can be tremendously mitigated. The NIR reflective pigments can be fabricated with four main approaches: sol-gel synthesis, solid-state route, precipitation, and hydrothermal method. Moreover, the effectiveness of the NIR reflective pigments can be evaluated via the cooling effect test after the pigments were prepared into coatings.

This section includes the impacts and countermeasures of the heat island effect, the popular synthesis methods of the NIR reflective pigments, the sol-gel synthesis of NIR reflective nanoparticles from different works, and also the cooling effect evaluation of the cool coatings which will provide the background information and highlight the importance of this work.

2.1 Overview of the Heat Island Effect

The heat island effect is a global problem since any urban area with human-made architecture absorbs the heat better than its environment. The effect might keep people warm in the winter, but more adverse effects impact society both directly and indirectly. The direct impact comes from the increased temperature, while the examples of the indirect impact are climate change and global warming, which are severe global environmental issues. The consequences of the heat island effect can be categorized into three aspects of human health and well-being, economic, and environmental.

2.1.1 Human Health and Well-Beings

Two factors that affect human health and well-being are the heat and the impacts of climate change. In this aspect, the heat island effect can be related to sickness, working performance, and the well-being of humans.

2.1.1.1 Sickness

2.1.1.1.1 Heat-Related Sickness With the increased global temperature and even higher in the urban area, the heat causes adverse health impacts from morbidity to mortality when the body core temperature reaches 38-39°C (Lundgren & Kjellstrom, 2013). Examples of heat-related illnesses are uneasiness, dehydration, anxiety, fatigue, dry skin, rapid heart rate, muscle aches, and heatstroke (RICC et al., 2020). In 1995, a heatwave caused 700 excess deaths in Chicago (Semenza et al., 1996). Similarly but more severe, in 2003, 15,000 heat-related deaths were reported in France from the 11-12°C increased temperature than the norm for nine consecutive days (Fouillet et al., 2006).

Some groups of people are more vulnerable to heat morbidity and mortality than others. The children, elderly, and chronic disease patients who have low heat tolerance and cannot care for themselves can be in danger from a heatwave or stay in a place with high temperature for a long time. Those required to work in the presence of a heat source or perform strenuous physical activities outdoors have a higher chance of being affected by the heat. Moreover, with lower socioeconomic status, the ability to acquire resources for heat mitigation and the healthcare system is lower (Li et al., 2015).

2.1.1.1.2 Vector-Borne Diseases Infectious diseases from vectors so-called 'vector-borne diseases' (VBDs) are the impacts of climate change. VBDs are sicknesses from bacteria, viruses, or parasites carried by an arthropod vector such as mosquitoes, bugs, flies, aquatic snails, and lice. Chikungunya, malaria, lymphatic filariasis, sleeping sickness, and plague are examples of well-known VBDs (Müller et al., 2019). Each year, there are more than 700,000 deaths from VBDs (WHO, 2020).

The change of climate, including the extended or shortened period of seasons and the temperature fluctuation, influences the evolution of pathogen–vector–host systems. The ambient rearing temperature directly affects the virus susceptibility and dissemination rate in the vector from the physiological processes in virus amplification. The regional change in temperature leads to new occurrences or the disappearance of the VBDs. The

new VBDs can cause serious infections in the unprepared society with low immune populations (Caminade et al., 2019; Fouque & Reeder, 2019).

2.1.1.1.3 Permafrost Disease Cold and frozen permafrost is the most suitable environment for the long-term survival of some microorganisms and plants, including infectious viruses such as Influenza (Tumpey et al., 2005) and Variola (Biagini et al., 2012) viruses (Legendre et al., 2014). Both stated viruses cause flu and smallpox pandemics across the world, respectively. Influenza virus develops itself into various species where people can be infected with mild or severe symptoms, unlike smallpox, in which 3 out of 10 infected people died. With the effort of international public health, the world was free from smallpox since May 8, 1980 (CDC, 2019, 2021).

Global warming increases the average temperature of the Earth's surface and sea, leading to permafrost melting. The organisms that survived the capture of the ice are then released out. The released viruses or bacteria might cause severe pandemic than what humans have ever faced before. Therefore, it is urgent to stop the permafrost from melting from the rise in global temperature.

2.1.1.2 **Mental and Physical Performances** Thermal comfort is one of the most critical factors that can affect working performance. A too low or too high temperature of the working site can reduce the working efficiency and lead to unproductive output, which wastes resources and time (Lipczynska et al., 2018). At raised temperature, adverse effects on the physiological mechanism of the human body are reported, including a rise in heart rate, a higher frequency of respiratory ventilation, the higher partial pressure of the CO_2 and lower O_2 in the blood. Such mechanism increases fatigue, mental workload, negative mood disturbance, and sick building syndrome, which people are less willing to put effort into their work (Lan et al., 2011). Therefore, the temperature of the working place dramatically impacts one's performance.

The heat absorption of human-made architecture increases the temperature of the buildings, which are the offices for urban populations. The heat island effect also escalates the overall temperature of the city. Therefore, tremendous cooling energy and spending are required (Kolokotroni et al., 2006).

2.1.1.3 **Well-Being** From heat, instead of spending for better well-being, the expenditure on cooling is increased due to the heat island effect. Higher quality of

equipment, better facilities, more self-development, or better education are examples of the well-being obtained from the saved budget.

Regarding climate change, natural disasters become more violent and fluctuated from the norm season. People's well-being can be affected directly by becoming homeless and poor after a natural catastrophe such as a flood or storm. Food and water scarcity are getting more severe as the global warming issue rises. Climate change is no longer a distant threat (Manning & Clayton, 2018). The problem is relevant to everyone since its impacts affect the whole globe.

2.1.2 Economic

The increased temperature and the effect of climate change slow down the economic growth described later in detail.

2.1.2.1 **Poverty and Inequality** People who live in vulnerable areas, low-income and tropical regions, have to face food and water scarcity which are getting more severe as the global temperature increases (Nordhaus, 2019). The coastal area's risk of being attacked by coastal flood and damage is higher because of the change in tropical cyclone frequency and intensity. Agricultural yields can also delay or spoil from a heavy monsoon. Some places might face drought such that the main earnings from agriculture cannot be obtained. Climate-related shocks can wipe all the accumulated assets of a household at once and lead to poverty. Therefore, climate change directly impacts poverty in vulnerable areas (Hallegatte & Rozenberg, 2017; Marotzke et al., 2020).

In addition, low socioeconomic background further limits the opportunity to acquire resources and creates inequality, forming a more significant gap between the rich and the poor. The cycle of poverty is endless without outside intervention. From the poor yield of agricultural products affected by climate change, the price of food increases which is unreachable to poor people. The poor have fewer resources and more chances to live in vulnerable areas, and this cycle continues as it is (Castells-Quintana et al., 2018).

2.1.2.2 **Economic Growth** The heat island effect increased urban and global temperature leads to difficulties and limitations in the economic aspect. The most affected part is the agricultural industry which depends on natural systems such as rain-fed and coastal farming. The temperature change might decrease the yield of

temperature-sensitive agricultural products (Marotzke et al., 2020; Morton, 2007). Industries which are depending on agricultural products are then affected by resource deficiency. Tourism activities have to be adapted according to the change in the environment. Natural sightseeing can be diminished along with the temperature change. Outdoor activities are more strenuous and exhausting in heat (Scott et al., 2019). Consequently, agricultural and related-field, tourism, and outdoor-related industries are troubled by the rise in temperature leading to the struggle for economic growth.

Similarly, owing to climate change, natural disasters can wipe out natural resources, destroy transportation routes in which the delivery is delayed where products are spoiled or went missing, and cease all activities from business as usual. Thereby, climate change also has direct adverse effects on the economic growth of every sector, from household to global scale.

2.1.3 Environment

More and more energy is required for cooling as the collected heat increases the city's overall temperature, especially in summer and the daytime. High energy consumption worsens climate change since up to 84% of the energy comes from burning fossil fuel and coal oil that release a vast portion of GHGs into the atmosphere (Ritchie & Roser, 2017). In addition, climate change further impacts natural resources since the environment is adapted according to the change in temperature and climate.

2.1.3.1 **Energy Intensity** Energy intensity indicates how much energy is required for converting into the output (EERE). Against the heat island effect, air conditioning is the standard solution for thermal satisfaction conditions in urban areas. Anthropogenic heat from energy consumption for human activities is the additional heat source (Du et al., 2016). Air conditioning can further increase the compacted urban region up to 2°C and worsen the urban heat island effect (Giridharan & Emmanuel, 2018).

The worldwide consumption of energy for air conditioning is rapidly increased by 70% from 2000 to 2100. In tropical regions, with climate change, an additional 50% more energy is required for air conditioning (Isaac & Van Vuuren, 2009). The energy intensity is considered too high and inefficient since the input energy significantly increases relative to the output.

In 2019, 64% of the electricity used for air conditioning came from fossil fuels, accounting for 75% of GHGs emissions (Ritchie & Roser, 2017). The emissions then deteriorate climate change, intensify its impacts on society, and create a vicious circle of global warming. When the GHGs are collected in the atmosphere, more heat is reflected back onto the Earth's surface and builds up a higher temperature in the urban.

2.1.3.2 **Natural Resource** Natural resources, including plants, animals, and water, are temperature and climate-dependent. Thereby, global warming directly affects the prosperity of natural resources. For plantation and farming, some adaptations are required because of the change in the climate pattern from its standard. For the reservation of forest and wildlife, resource monitoring, management, and restoration plans can help mitigate the effect of extreme weather events which are more vigorous from climate change, such as a severe drought or wildfire in summer. Technologies and strategies are required, such that agriculture does not depend entirely on the natural system and can maintain water supply to all trees and wildlife living in the forest (Morton, 2007; Peterson & Halofsky, 2018).

Most of the extra cooling energy against the heat island effect comes from natural resources, which are fossil fuels. Around 1980, the consumption of fossil fuels significantly increased, as shown in **Figure 2.1**. Fossil fuels can be categorized into coal, oil, and gas, which are all non-renewable resources. Even though there is no solid evidence, the depletion of fossil fuel reserves could be a pressing issue in around 50-100 years. Moreover, the energy production from fossil fuels is not healthy for the climate from the GHGs emissions during the combustion processes (Ritchie & Roser, 2017; Tauseef Hassan et al., 2021).

Figure 2.1

The Graph Shows Global Fossil Fuel Consumption From 1800 to 2019 (Roser, 2020)

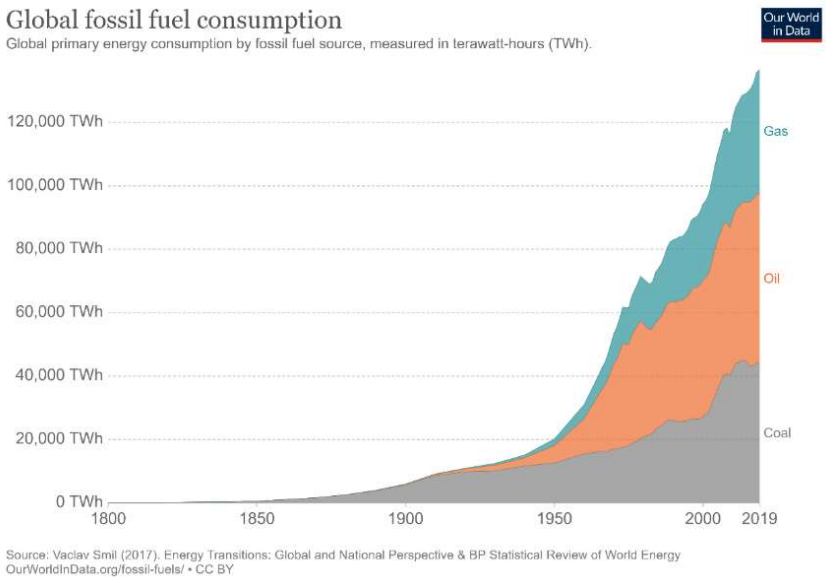

2.1.3.3 **Climate Change** Greenhouse gases (GHGs) are the atmospheric gases keeping the heat radiation from the Sun inside the atmosphere, warming up the Earth's surface so that life is livable. However, due to human activities, GHGs rapidly increased, leading to the excessive heat collected in the atmosphere, as shown in **Figure 2.2** or so-called 'global warming'. One activity that releases an enormous amount of GHGs is the energy production from burning fossil fuels mentioned in this chapter.

Figure 2.2

The Graph Shows the Earth's Surface Temperature and the Atmosphere in the USA From 1900 to 2020 (EPA)

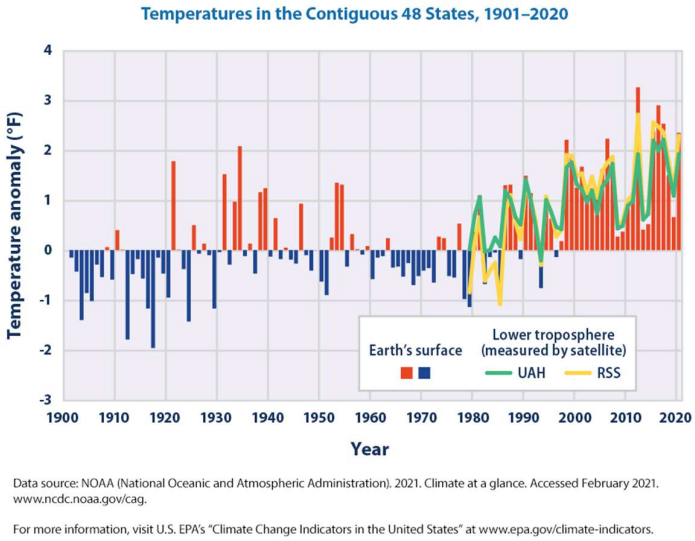

The cooling attempts against the heat island effect caused increased energy usage and fossil fuel combustion. The global warming situation induces climate change and intensifies the severity of natural disasters.

The heat island effect increases the urban area's overall temperature, causing heat-related sickness, low working performance, and poor well-being. The heat also exacerbates the poverty and inequality issues in society and slows down economic growth. The energy required for cooling is escalated, leading to the high expense and rapid consumption of natural resources. In addition, energy production produces enormous GHGs that worsen climate change and intensify its impacts on society. The summary of societal implications is shown in **Figure 2.3**. Accordingly, the heat island effect is a vital problem to be mitigated and solved for the better well-being of society.

Figure 2.3

The Figure Summarizes the Societal Implications of the Urban Heat Island Effect

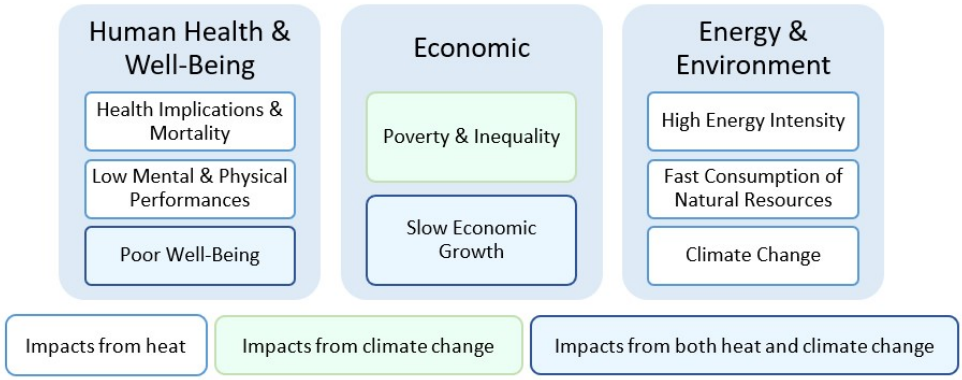

2.2 Countermeasures of the Heat Island Effect

Numerous methods for the heat island effect and climate change mitigations are applied to buildings and infrastructures in urban areas. The countermeasures can be categorized into four categories: city design, green infrastructures, NIR reflective structures, and policy. **Figure 2.4** summarizes how each countermeasure helps with the mitigation, and **Table 2.1** summarizes the advantages and disadvantages of each mitigation. Accordingly, all methods have to be carried out to efficiently mitigate the heat island effect, as mentioned in the details listed later on.

Figure 2.4

The Figure Identifies How Each Countermeasure Mitigates the Impacts of the Heat Island Effect

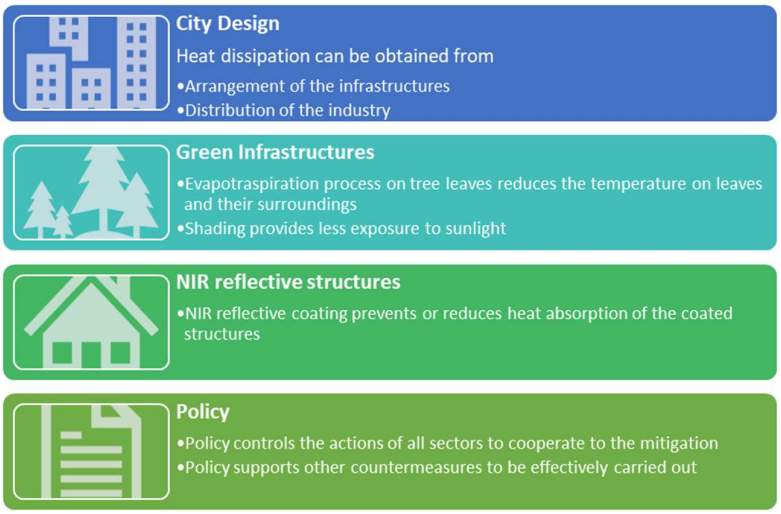

Table 2.1

The Table Summarizes the Advantages and Disadvantages of Countermeasures for the Heat Island Effect

Counter-measures	Advantages	Disadvantages/Limitations
1. Urban design	- Provide long-term impact	- Take time for research and design - High cost of reestablishment - The design might not be appropriate for seasons other than summer
2. Green infrastructure	- The trees can be counted as a decoration component for the city - Green colors give comfort to the eyes	- High cost of plantation establishment, watering, and maintenance - Poor attention can cause dirtiness from leaves and wildlife debris
3. NIR reflective structures	- Can be coated on any surface - The dark color is possible with the use of nanotechnology	- Nanotoxicity
4. Policy	- Provide a high impact on every sector of the society	- Corruption can lead to the ineffectiveness of the policy - The regulations only depend on the government

2.2.1 City Design

Urban design is a fundamental approach to reducing heat from the heat island effect since the absorbed heat intensity depends on the land cover types. Materials used in urban are asphalt, tile, and concrete, which have high heat flux and thermal inertia, so the heat can be collected better than on natural surfaces (Guo et al., 2015). With an appropriate design and distribution of the infrastructures and industries, the heat can be dissipated efficiently, and the city's overall temperature is reduced. In addition, with the construction of ecological corridors, the mass and energy exchange can be facilitated better than in a compacted area of buildings (Du et al., 2016).

Another factor is urban geometry. The aspect ratio of urban street canyons or the canyons created from a street flanked by buildings on both sides is an essential factor

in determining the pedestrian area's temperature. The higher aspect ratio of high buildings with a narrow street provides more shading and higher wind velocity to the pedestrian, leading to thermal comfort in summertime. However, the lower solar exposure is a disadvantage in the winter.

East-West street orientation is the worst design for thermal comfort since the street is exposed to sunlight all day where the increased temperature can be as much as 25.1°C. A good street orientation can offer shading and wind to reduce thermal discomfort. Some studies reported that 451° is the optimal degree between the street and the wind direction between the canyon (Jamei et al., 2016). Therefore, selecting the desired orientation of the road and buildings is complicated and burdensome.

Organized urban sections and facilitated public transport can reduce anthropogenic heat and GHGs emissions from private transportation. An appropriate design of a city plan supporting pedestrians can also reduce the number of personal vehicles.

Nevertheless, designing the appropriate distribution and composition requires time for research and planning. Moreover, changing urban design after the finished construction is considered extravagant for both the construction budget and resources. Consequently, the urban plan for the heat island effect mitigation might not be suitable for urbanized areas full of buildings and constructions but apt for the new city preparing to be built.

2.2.2 Green Infrastructures

Green infrastructures such as street trees, urban parks, and green roofs are the crucial components in reducing the collected heat by evapotranspiration and shading. Evapotranspiration is when the water absorbs heat, evaporates from tree leaves, and cools down the leaves and their surroundings (Jamei, Rajagopalan, Seyedmahmoudian, & Jamei, 2016). Compared to the non-shaded area, the temperature is lower with tree shading, which reduces the energy load for cooling with air-conditioning. Planting large trees near houses helps reduce cooling energy by up to 21-53% (Akbari et al., 1997). Urban parks are also essential components of the city. Park cool island is a phenomenon where the green areas have 1-7°C lower in temperature the green park acts as a heat sink and source of cool breeze in the city (Jamei et al., 2016). With computer simulations, annual space cooling costs can be saved by 53-61% by dense shade all over the surface, and up to 32-49% of peak cooling loads can be reduced (Gago et al., 2013).

The roof area accounts for 20-25% of the dense city, considered a large area. Therefore, green roofs or living roofs covered with vegetation are another heat island effect mitigation for multi-story buildings, single-family residences, and other buildings with available roof space. The efficiency of the green roofs can reduce the annual energy load by 1-40% depending on their design, local climate, and characteristics of the building. The thickness and type of plants are directly related to the heat transferred to the roof.

Apart from the evapotranspiration process, watering is another factor that reduces the latent heat released from the roof surface. The impacts of green roofs are higher in non-insulated buildings than the insulated ones since the temperature under the insulated structures is slightly related to external factors. In addition to mitigating the heat island effect, green roofs also have advantages of increased roof material durability, stormwater management, better air quality, noise reduction, and offering space to urban wildlife (Santamouris, 2014).

Still, taking care of and maintaining the trees have a high cost (Akbari, 2005). Water restrictions from extended droughts or prolonged big floods in the city might lead to damaged street trees and green parks, requiring further restoration. In the case of green roofs, poor attention and management might lead to damage from roots penetration into the waterproof infrastructures and dirtiness from wildlife living on the vegetation. Moreover, with packed buildings and busy streets, the green infrastructures might not be enough to significantly reduce the city's temperature for thermal comfort (Jamei et al., 2016).

2.2.3 NIR Reflective Infrastructures

Cool or reflective infrastructures are the structures applied with the albedo or NIR reflective coatings with higher heat reflectivity than bare surfaces. NIR reflective coatings can be used on any surface such as roof, glass, pavement, and concrete. The first generation is the natural liquid-applied materials with a maximum 0.75 albedo value. The obtained second generation has around 0.85 albedo value from the artificial white material. Colored material with higher NIR reflectivity is the third generation that can simultaneously provide color and heat reflectivity. Lastly, the fourth generation composes of nanomaterial, which provides even higher reflectivity to the NIR radiation

such that the color of the coating can remain dark with low heat absorption (Akbari, 2005; Santamouris, 2014).

With highly thermal absorptive structures, the temperature difference between the ambient air and the surface can be up to 50°C, while the surface coated with albedo coating has only a 10°C difference. Several studies reported that NIR reflective coating could save energy 5-46% depending on the season, location, and type of building. Cooler temperature also leads to a longer lifetime of the material, which means that the cost of restoration is also reduced since the degradation of materials usually depends on the absorption of ultraviolet light, a temperature-dependent process (Akbari, 2005).

NIR reflective coating can be applied on any surface with the desired color since the color can be adjusted without affecting the reflectivity with the help of nanotechnology. The coating might increase the cost of painting. However, with further development, the last-long coating can be obtained such that there is no need to reapply for a long time, and the cost will be reduced with large-scale production.

One downside of this approach is the toxicity of the nanomaterials. Without care and attention, exposure to a high concentration of nanomaterials can lead to adverse effects on human cells, such as DNA and cell damage (Y.-W. Huang et al., 2017).

Even though there is not enough study reported about the apparent impacts of nanotoxicity on the human body, direct exposure to nanomaterials must be avoided, especially for the researchers, manufacturers, and painters. However, after the coating is dried, the nanomaterials are locked inside the coating, and the leaking from weathering is considered to have a very low concentration (Llana et al., 2021).

2.2.4 Policy

The policy is a tool for governments to guide and control the actions of all sectors, including government, city administration, inhabitants, and private sectors. The overarching areas for mitigation of heat islands include the landscape and urban form, green and blue area ratio, albedo enhancement, transport modal split, and public health (Degirmenci et al., 2021).

As mentioned in the urban design part, urban infrastructures and their arrangements have a significant impact on the heat dissipation of the city. Therefore, the policy can manage the ratio of buildings, streets, spaces, trees, and water bodies appropriate for

heat dissipation (Degirmenci et al., 2021). Research showed that a smart growth policy impacts the heat island effect of the sprawl development scenario. Therefore, the initial planning policy for the neighborhood is more important than the policies to be adopted later since there is only a slight chance to reshape the developed city (Deilami & Kamruzzaman, 2017).

Public transportation is another means to mitigate the GHGs emission from vehicles. A modal split assisted by policy can be obtained from the public transportation options which support citizens to travel via public transport rather than private vehicles (Degirmenci et al., 2021).

Another essential part is the policy support for the mitigation technology such as albedo enhancement and energy consumption, heating, ventilation, and air conditioning (HVAC) system. With advanced technology, the mitigation of the urban heat island effect is more effective. For example, 99.11% of the NIR reflectivity can be obtained from coating to reduce the amount of heat absorbed by human-made infrastructures such that a massive amount of cooling cost can be reduced (B. Huang et al., 2017). The high efficiency of the HVAC system also reduces the energy demand for cooling. Therefore, funding and supporting research can build a very high impact on the heat island effect mitigation.

Nonetheless, corruption is the most troublesome problem, which always slows down the development of policy. When the funding is misapplied, the policy cannot be delivered efficiently such that the mitigation is not carried out successfully.

2.3 Fabrication of NIR Reflective Pigments

Among all of the countermeasures for the heat island effect mitigation, NIR reflective coating is the technology response that all sectors in society can take part in and can be further developed for better effectiveness of the heat island effect mitigation. To develop the NIR reflective coating, NIR reflective pigments are fabricated with mainly four approaches the solid-state route, precipitation method, hydrothermal method, and sol-gel synthesis. The advantages and disadvantages of each approach are summarized in **Table 2.2**, and the details are further listed in the sub-sections.

Table 2.2

Advantages and Disadvantages of Each Fabrication Method of the NIR Reflective Pigments

Method	Advantages	Disadvantages
1. Solid-State Route	- Environmentally friendly - Easy to control the crystallite size - Non-toxic	- High working temperature - Require equipment that can withstand high temperature - High energy consumption - Could be time-consuming
2. Precipitation	- No solid waste - Provide different shades of colors	- Equipment demand for simultaneous employment of precursors - High energy demand
3. Hydrothermal	- Single-step process - High degree of crystallinity and phase homogeneity, narrow size distribution, and high purity of the product	- Toxic waste releasing
4. Sol-Gel	- Simple - Low working temperature - Low cost - Environmentally friendly	- Could be time-consuming - Unavailability of suitable precursors

2.3.1 Solid-State Route

The solid-state route includes the process of mechanical mixing and requires conditions of high temperature and long soaking time. The precursor oxides are mixed, poured into a mortar, and underwent wet milling until homogenized in the solvent of acetone/ethanol/water. The solvent is then evaporated. The powders are calcined at a specific temperature and time in the air with a furnace. The final pigment is grounded for further characterization (Jose et al., 2019).

The solid-state synthesis can be tuned to provide the desired crystallite size of the pigments. It doesn't create harmful products. Therefore, it is an environmental-friendly process, and the process is also non-toxic. However, the process requires high-temperature treatment in the range of 500-2000˚C, which is energy consuming, expensive, and requires equipment that can withstand high temperatures. This approach requires the highest temperature compared to other techniques mentioned in this report.

Moreover, the total reaction time can be several days, with the grinding in between to obtain the homogeneous reaction mixture (Jose et al., 2019; Rosati et al., 2021).

2.3.2 Precipitation Method

Coprecipitation is a popular approach to synthesizing metal-oxide nanoparticles by slowly mixing precursors simultaneously at elevated temperatures for a specific time until a precipitate is formed. The precipitate is then filtered for further heat treatment and calcination (Athar, 2015).

The coprecipitation approach is an environmentally friendly process since it doesn't create any solid waste where all precursors are facilitated efficiently and doesn't require any organic solvent. The fabricated pigments could be in various shades of colors from the number of input precursors. However, significant limitations of this approach are the equipment demand for the simultaneous addition of precursors and energy demand during the process (Rosati et al., 2021).

2.3.3 Hydrothermal Method

The hydrothermal approach is a synthesis method via chemical reactions in a liquid state at elevated temperatures and pressure. The precursors are mixed together before treating with high temperatures and pressure, generally with an autoclave (Xu et al., 2018).

The hydrothermal method is a single-step process that requires low process temperature such that the processing time is short and needs low energy input. The product from this approach can obtain a high degree of crystallinity, phase homogeneity, narrow size distribution of the particles, and high purity. However, the facilitated temperature is still high compared to the sol-gel synthesis, and there might also be a toxic liquid waste release (Rosati et al., 2021).

2.3.4 Sol-Gel Synthesis

The sol-gel synthesis is a simple wet chemical approach that can ensure the homogeneity of the product. Sol is the colloidal suspension of small particles with Brownian motion, and gel is the network of the solid particles in the continuous liquid phase after the solvent is evaporated. After the precursors are suspended until the homogeneous mixture is obtained, the mixture is heated with constant stirring to evaporate the solvent until the gel is formed. Then, the gel goes through a heat treatment in the range of 100-200˚C to obtain the powder form, followed by the calcination

process at a high temperature from 300-900˚C to get the final product (Jose et al., 2019; Rosati et al., 2021).

Due to the preparation in a liquid phase, the precursors can be suspended throughout the solution. The gel obtains high homogeneity, which prevents the agglomeration of the nanoparticles; thus, the NIR reflectivity is enhanced. This approach makes it easy to control the final product's purity, composition, and microstructure. Moreover, the process is also simple, low cost, and environmentally friendly since it has no requirement for a high-temperature process. Nevertheless, the disadvantages are the unavailability of suitable precursors and the different hydrolysis susceptibilities of each component since the advantage of homogeneity can be lost during the hydrolysis of alkoxide materials (Jose et al., 2019).

2.4 Sol-Gel Synthesis of NIR Reflective Nanoparticles

The sol-gel technique is used in this research because of its simplicity, low cost, lack of high-temperature process, and lack of sophisticated equipment. This section collects works of synthesizing core-shell nanoparticles with the sol-gel technique. The core materials are Cr_2O_3, Al_2O_3, and Fe_2O_3. The literature review will only focus on synthesizing the TiO_2 shell to the metal oxides cores, which titanium tetraisopropoxide (TTIP) and tetrabutyl orthotitanate (TBT) are two primary sources of the Ti.

The sol-gel approach includes hydrolysis, condensation, and heating process. Hydrolysis, alcohol condensation, and water condensation reactions are listed in **Equations 2.1**, **2.2**, and **2.3** respectively.

$$Ti - \{OCH(CH_3)_2\}_4 + xH_2O \rightarrow Ti - \{OCH(CH_3)_2\}_{4-x}(OH)_x + xCH(CH_3)_2OH \quad 2.1$$

$$\equiv Ti - OCH(CH_3)_2 + HO - Ti \equiv \rightarrow \equiv Ti - O - Ti \equiv + CH(CH_3)_2OH \quad 2.2$$

$$\equiv Ti - OH + HO - Ti \equiv \rightarrow \equiv Ti - O - Ti \equiv + H_2O \quad 2.3$$

2.4.1 Sol-Gel Synthesis of Cr_2O_3-TiO_2 Core-Shell Nanoparticles

For the synthesis of Cr_2O_3-TiO_2 core-shell nanoparticles, the work can be rarely founded. Tan et al. worked on a five-step process, from synthesizing Cr_2O_3 nanoparticles to calcination of the TiO_2 shell (Tan et al., 2019).

At first, the SiO_2 layer was formed as a shell to prevent the aggregation of Cr_2O_3 nanoparticles. Cr_2O_3-SiO_2 nanoparticles were dispersed in ethanol before slowly adding TBT into the solution to form Cr_2O_3-SiO_2-TBT nanoparticles. Then, the SiO_2 layer was replaced with TiO_2 by an alkaline hydrothermal etching-assisted crystallization method. After that, the Cr_2O_3-titania core-shell nanoparticles were dried in an oven at 75˚C and calcined at 400, 550, 700, and 850˚C to obtain Cr_2O_3-TiO_2 core-shell nanoparticles.

The work aimed to synthesize Cr_2O_3-TiO_2 core-shell nanoparticles for the photocatalytic reduction of CO_2. Therefore, there is no NIR reflectivity test on the product. The size of the core-shell nanoparticles is around 90nm, as shown in the SEM image and elemental line scan in **Figure 2.5**.

Figure 2.5

SEM Image (d) and Elemental Line Scan (i) of the Cr_2O_3-TiO_2 Core-Shell Nanoparticles Fabricated in Tan et al. (Tan et al., 2019)

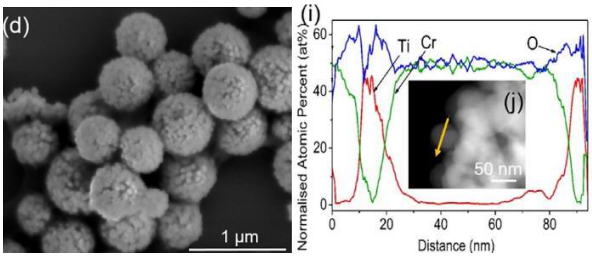

2.4.2 Sol-Gel Synthesis of Al_2O_3-TiO_2 Core-Shell Nanoparticles

Yang et al. fabricated Al_2O_3-TiO_2 core-shell structures for the absorption of SO_2 and NO pollutants. Two solutions of dispersion and TBT were prepared separately (Yang et al., 2019). The dispersion of Al_2O_3 nanoparticles was then dropwise added to the TBT solution under mechanical stirring at 40˚C until gel was formed. The gel was then dried at 110˚C for 12 hours before calcination at 500˚C for 6 hours. The porous Al_2O_3-

TiO_2 core-shell structures were obtained with a diameter of around 200nm and pore size of 10nm.

Similarly, Yi et al. (Yang et al., 2019) synthesized Al_2O_3-TiO_2 core-shell structures absorbents by preparing TTIP solution, then added Al_2O_3 nanoparticles under continuous stirring. The mixture was homogenized with 24,000rpm for 1 hour before aging at room temperature for 48 hours until gel was formed. The gel was dried in an oven at 120˚C for 4 hours before calcination at 500˚C for 5 hours. However, there is no report of the morphological or NIR reflective properties.

Another work from Karunakaran et al. fabricated Al_2O_3-TiO_2 core-shell nanoparticles with a straightforward process (Karunakaran et al., 2015). After Al_2O_3 nanoparticles were dispersed in ethanol, an emulsifier was added to the solution, preventing the nanoparticles' agglomeration. TTIP was then added, and the solution was under continuous stirring until the gel was formed. Drying and calcination at 120˚C for 6 hours and 500˚C for 3 hours then proceeded. The results of EDX and XRD confirmed the structure of Al_2O_3-TiO_2 nanoparticles with a size of around 90-120nm, as shown in **Figure 2.6**.

Figure 2.6

SEM Image of the Al_2O_3-TiO_2 Nanoparticles from Karunakaran et al. (Karunakaran et al., 2015)

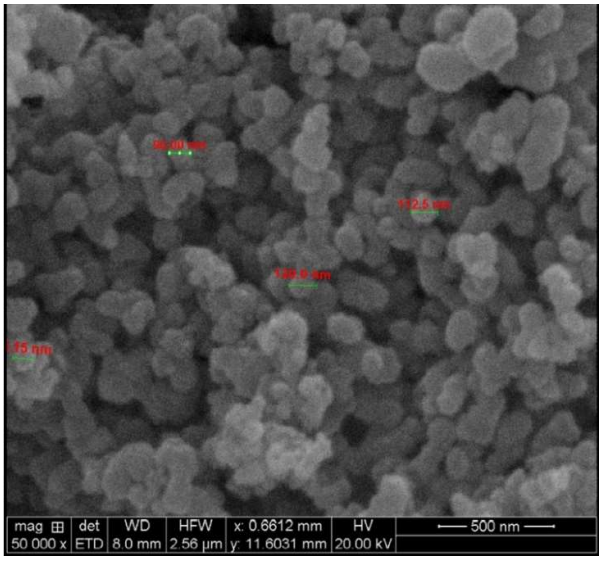

2.4.3 Sol-Gel Synthesis of Fe_2O_3-TiO_2 Core-Shell Nanoparticles

Sadeghi-Niaraki et al. fabricated Fe_2O_3-TiO_2 core-shell nanoparticles for NIR reflective and photocatalytic applications (Sadeghi-Niaraki et al., 2019). The synthesis started with the dispersion of Fe_2O_3 nanoparticles in the solution of acetone, ethanol, and ammonia. TBT was then added to the solution, which was further stirred at 600rpm for 2 hours. After centrifuge at 3000rpm followed by washing with ethanol and DI water several times, the sample was dried at 80˚C for 12 hours and calcined in air at 600˚C for 2 hours. The schematic illustration of the process is shown in **Figure 2.7**. The ratio of 0.06 Fe_2O_3/TiO_2 provided the highest NIR reflectance of 73%, with the nanoparticle size around 400-500nm. With the increased proportion of Fe_2O_3/TiO_2, the aggregation of Fe_2O_3 nanoparticles was investigated, as shown in **Figure 2.8**, where CFT2, CFT4, and CFT5 are the Fe_2O_3-TiO_2 core-shell nanoparticles with Fe_2O_3/TiO_2 ratio of 0.06, 0.62, and 1.24 accordingly. The reflectivity of the pigments also decreased as the proportion increased.

Figure 2.7

Illustration of Fe_2O_3-TiO_2 Core-Shell Nanoparticles Formation (Sadeghi-Niaraki et al., 2019)

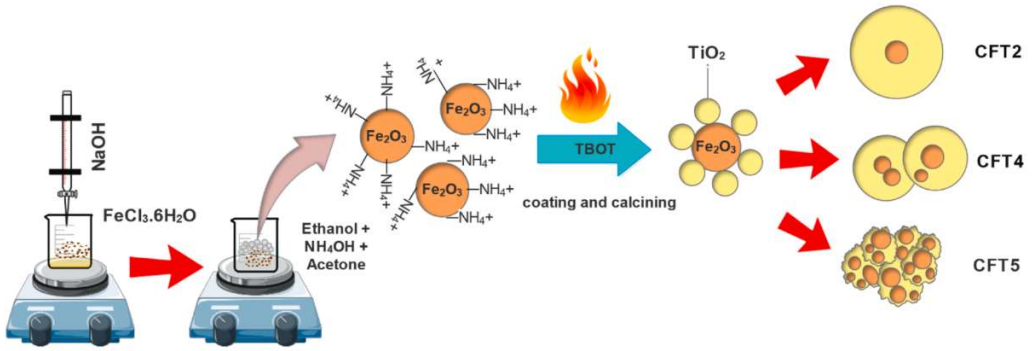

Figure 2.8

SEM Images of the Fe_2O_3-TiO_2 Core-Shell Nanoparticles with the Fe_2O_3/TiO_2 Ratio of 0.06 (f), 0.62 (g), and 1.24(h) (Sadeghi-Niaraki et al., 2019)

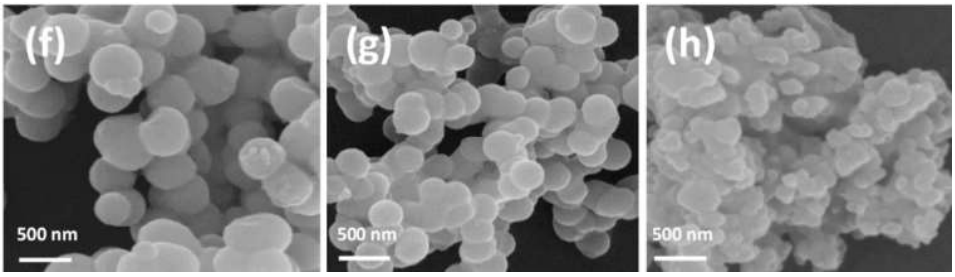

Chen et al. fabricated Fe_2O_3-TiO_2 nanoparticles by adding Fe_3O_4 suspension to the solution of TBT prepared in ammonium and ethanol (CHEN et al., 2013). The synthesized particles were collected with a magnet instead of a centrifuge, dried in air for two days, and calcined at 450˚C for 4 hours. The resulted nanoparticles are shown in **Figure 2.9**. Another similar protocol from Kim et al. used a shorter time and higher temperature (Kim et al., 2016). After the solution was centrifuged and dried at 70˚C overnight, it was calcined for 2 hours with a temperature range of 500-800˚C. The mesoporous core-shell Fe_2O_3-TiO_2 nanostructures were obtained for photocatalytic applications, shown in **Figure 2.10**.

Figure 2.9

TEM Images of Fe_2O_3-TiO_2 Nanoparticles Fabricated in CHEN et al. (CHEN et al., 2013)

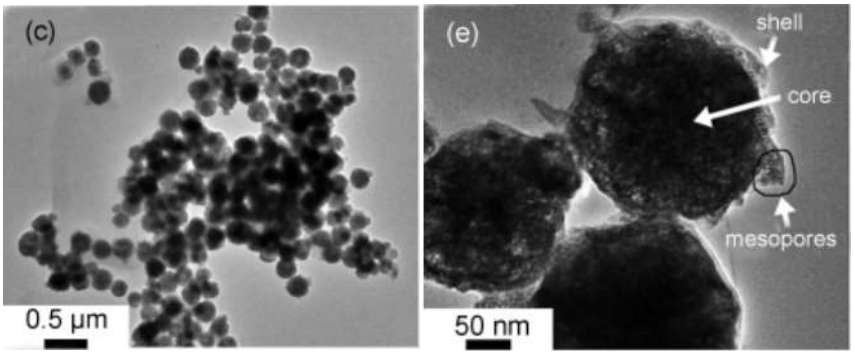

Figure 2.10

SEM (c) and TEM (d) Images of the Fe_2O_3-TiO_2 Nanoparticles Fabricated in Kim et al. (Kim et al., 2016)

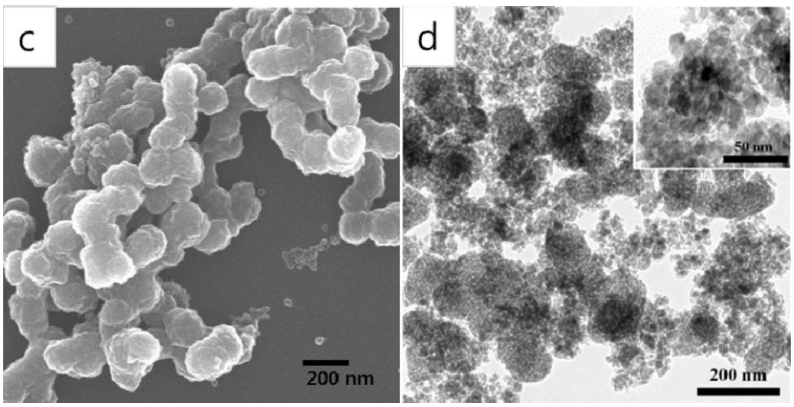

2.5 Cooling Effect Evaluation

The NIR reflectivity of the pigments can be evaluated directly by using a spectrophotometer. However, in practice, the application of the NIR reflective coatings on surfaces can be simulated by the cooling effect test which can evaluate the actual temperature change. Normally, the temperature difference between reference and NIR reflective coating is used for determining the reduced heat from the cool coating. The cooling effect test could perform both indoors under NIR radiation and outdoors under the sunlight. The outdoor cooling effect test is impacted by many factors such as air ventilation, the thermal conductivity of the substrate, and time of light exposure.

Malshe et al. evaluated the commercially available IR reflective inorganic pigments using an indoor setup as shown in **Figure 2.11**. Pigments were dispersed in styrene-acrylic emulsions with 50% solids as a binder. The pigment to binder ratio was 1:1. The coatings were then applied on a 6mm thick cement roof sheet. The light source was Philips 250W, 220-230V IR lamp, and the distance between the panels and light source was fixed at 30cm. A thermocouple was attached to the back of the panels to record the temperature. The temperature difference between the coated and uncoated panels was then calculated after 1 hour of light exposure. The temperature difference varied from -1 to 20˚C (Malshe & Bendiganavale, 2008).

Figure 2.11

Experimental Setup for Cooling Effect Test with an IR Lamp (Malshe & Bendiganavale, 2008)

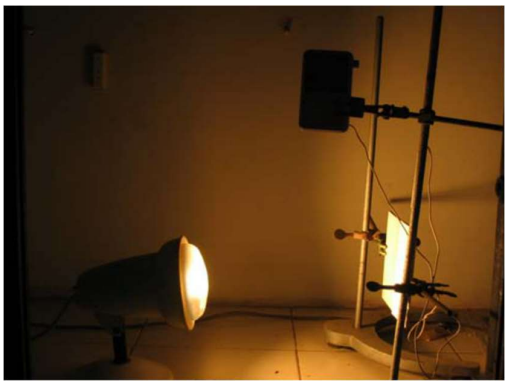

An outdoor cooling effect test was performed on NIR reflective green pigment based on Cr_2O_3 mixed with TiO_2, Al_2O_3, and V_2O_5 with different compositions. The highest 82.8% NIR reflectance of the mixture was obtained. Two identical house models were built from an iron frame with a 1m × 1m × 1m dimension as shown in **Figure 2.12**. 7mm-thick gypsum boards were the materials for walls and floor. The outer walls were coated with white paint. The inner walls and floor were insulated with 2 inches of polyurethane. The ceramic tile roof was coated with the NIR reflective green pigment compared with the commercially green pigment. K-type thermocouples were used for temperature measurement on the surface of roof tile, under the surface of roof tile, and at the center of the houses. The recorded temperatures from the model with NIR reflective samples were lower than the model coated with commercially paint from 1.3-2.5˚C as shown in **Figure 2.13** *(Thongkanluang et al., 2011)*.

Figure 2.12

Full Setup for an Outdoor Cooling Effect Test of the NIR Reflective Green Pigments (a) and Commercially Green Pigment (Thongkanluang et al., 2011)

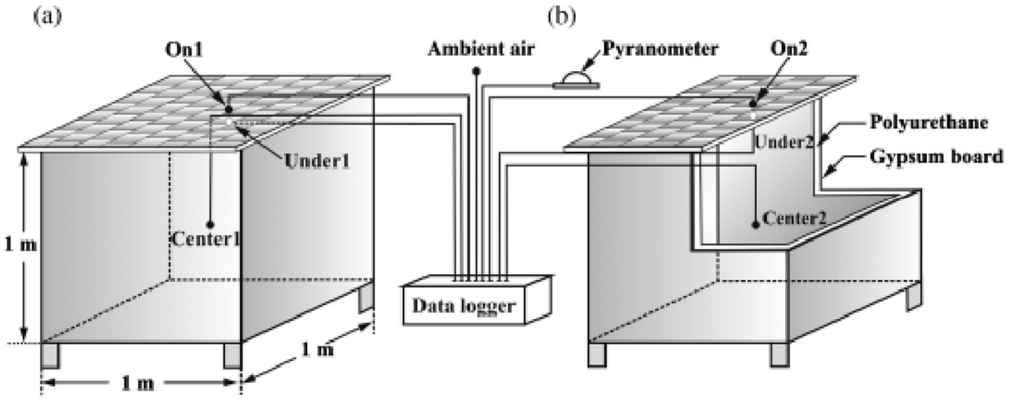

Figure 2.13

Temperatures Obtained from the House Models Coated with the NIR Reflective Paint (S9-coated) and the Commercial Paint (F-coated) (Thongkanluang et al., 2011)

			On the roof (°C)			Under the roof (°C)			Center of the room (°C)		
February	Ambient air (°C)	Solar irradiance (W/m^2)	S9-coated	F-coated	ΔT	S9-coated	F-coated	ΔT	S9-coated	F-coated	ΔT
24	33.9	866.4	51.7	53.9	2.2	50.9	53.2	2.3	43.3	45.1	1.8
25	33.1	877.2	49.9	51.4	1.5	49.1	51.1	2.0	41.2	43.1	1.9
26	33.6	849.9	51.1	52.6	1.5	49.7	51.4	1.7	42.4	44.4	2.0
27	32.8	938.3	50.2	51.5	1.3	48.6	50.8	2.2	41.5	43.4	1.9
28	32.9	950.1	50.3	52	1.7	48.5	50.7	2.2	40.9	42.5	1.6
Average	33.3	896.4	50.7	52.6	1.6	49.0	51.5	2.5	41.8	43.7	1.8

Xiang et al. conducted the cooling effect evaluation of cool materials under sunlight using a novel and facile sandwich structure device as shown in **Figure 2.14**. Cool materials were HDPE composites. The device was designed to be a thermally insulated cylinder such that the internal temperature was not affected by outside environments. After placing samples on the devices, the temperatures inside were recorded and compared to the references. The samples were left under the sunlight for up to 1 hour where it can be observed that the temperature was equilibrated as shown in **Figure 2.15**. The results show that HDPE/Green 260 could reduce the temperature inside by 5°C

lower than a neat HDPE even though the total solar reflectance (TSR) of HDPE/Green 260 is only 16.2% which is lower than the neat HDPE with 28.1% TSR (Xiang et al., 2015). This work indicates that determining only reflectance values is not sufficient and the cooling effect test is significant for the reflectance evaluation of the cool coating.

Figure 2.14

The Cross-Section View (left) and the Schematic Diagram of the Test Method (right) (Xiang et al., 2015)

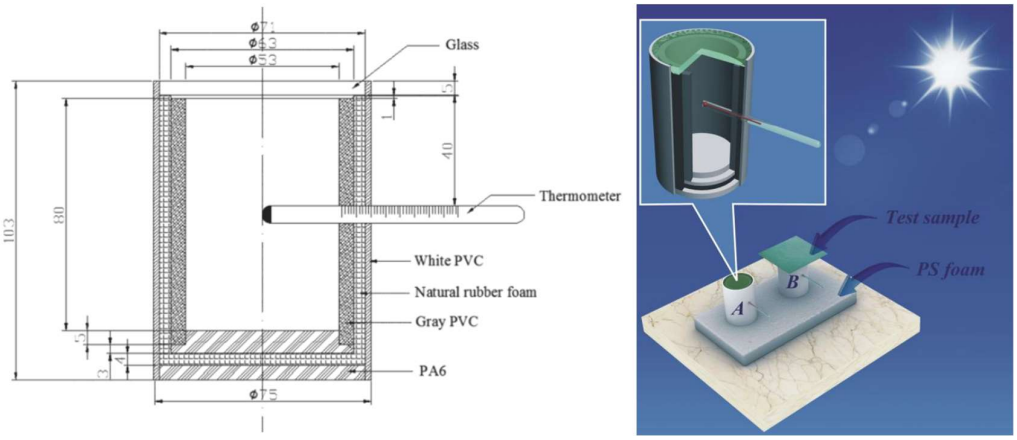

Figure 2.15

The Internal Temperature of the Device Over Time (Xiang et al., 2015)

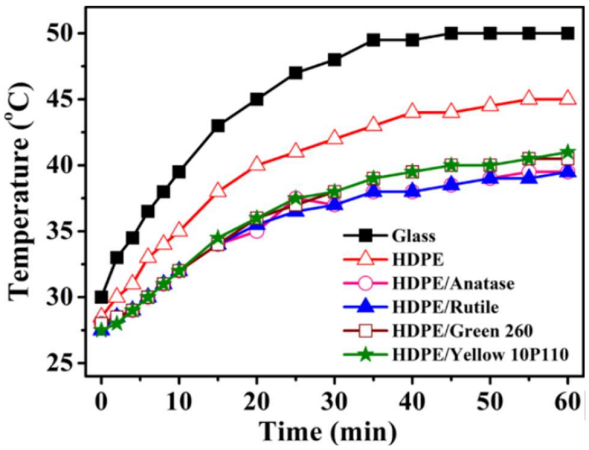

Qi et al. modified the surface of acrylonitrile-styrene-acrylate (ASA) with four types of TiO_2 to increase the solar reflectance and heat insulation properties. The ASA resin is a matrix material that provides excellent weather resistance. Fout types of TiO_2 are hydrophobic rutile nano-TiO_2 (A), hydrophilic anatase TiO_2 (B), unmodified rutile TiO_2 (C), and unmodified anatase TiO_2 (D). The hybrid materials provide higher NIR and solar reflectance from 26.2% and 43.3% to 63% and 70.9% for ASA/unmodified rutile TiO_2. For other samples, the reflectances were listed in **Figure 2.16**. Moreover, the indoor and outdoor cooling effect tests were conducted using a similar device as mentioned in the previous work of Xiang et al. in **Figure 2.14**. The temperatures detected under the hybrid materials are lower than the control ASA matrix around 5-10˚C for both indoor and outdoor tests where the temperatures were saturated after 1 hour after being exposed to the light source as shown in **Figure 2.17** for indoor and **Figure 2.18** for outdoor *(Qi et al., 2017)*.

Figure 2.16

Reflectance of Control ASA and ASA/TiO_2 Hybrid Materials: (A) Hydrophobic Rutile Nano-TiO_2, (B) Hydrophilic Anatase Nano-TiO_2, (C) Unmodified Rutile TiO_2, (D) Unmodified Anatase TiO_2. The TiO_2 particles are at 5 wt% Concentration in the ASA Matrix (Qi et al., 2017)

Samples	Reflectance/%			
	R_{UV}	R_{vis}	R_{NIR}	R_S
Control	32.0	65.4	26.2	43.3
A	17.9	81.5	45.2	59.4
B	14.4	70.2	42.1	52.8
C	10.7	87.5	63.0	70.9
D	19.1	87.4	58.6	69.0

Figure 2.17

The Cooling Property of ASA and ASA/TiO_2 Hybrid Materials Tested Indoors: (A) Hydrophobic Rutile Nano-TiO_2, (B) Hydrophilic Anatase Nano-TiO_2, (C) Unmodified Rutile TiO_2, (D) Unmodified Anatase TiO_2. The Ambient Temperature is 30 °C (Qi et al., 2017)

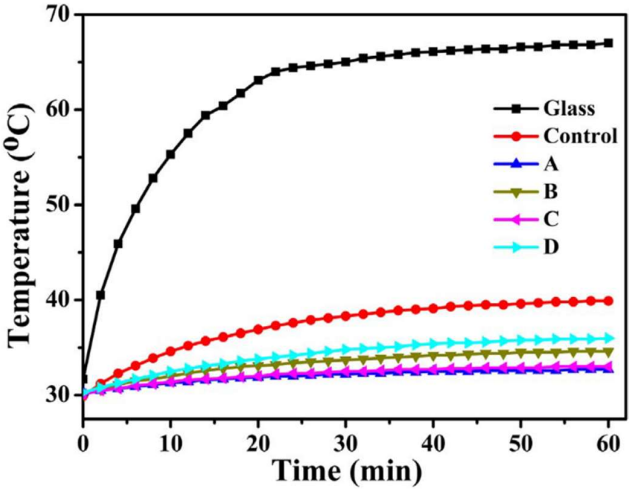

Figure 2.18

The Cooling Property of Pristine ASA and ASA/TiO_2 Hybrid Materials Tested Outdoors: (A) Hydrophobic Rutile Nano-TiO_2, (B) Hydrophilic Anatase Nano-TiO_2, (C) Unmodified Rutile TiO_2, (D) Unmodified Anatase TiO_2. The Temperature Test was Performed at 13:00–14:00 (1 h) on 29th July 2015, With an Ambient Temperature of Around 37 ° C. (32 ° 4 ′ 37 ″ N, 118 ° 46 ′ 19 ″ E, Nanjing, China) (Qi et al., 2017)

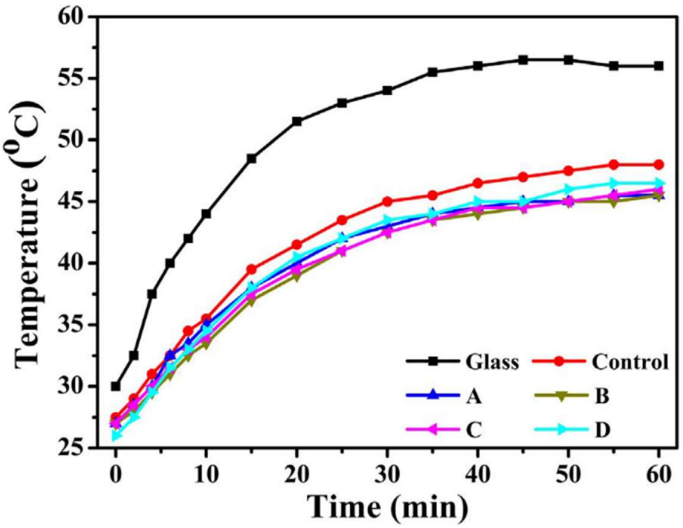

NIR reflective pink pigment was fabricated from Cr-doped alumina using the combustion method by Ianoș et al.. The TSRs of the pigment and coating are 69.2% and 61.7%. The pigment was then mixed with water-based acrylic emulsion with 20% mass pigment and coated on a 60mm×60mm aluminum sheet by a block applicator with a 300μm gap size. The coating thickness was 150μm. The coating was put under an IR lamp at a 20cm distance for 30 minutes as shown in **Figure 2.19**. FLIR T640 IR camera was used for the thermal imaging with 15 frames/s. With the same setup, reference materials, which were black carbon-based coating and white TiO_2-based coating, also underwent the cooling effect test. The surface temperature of the pink coating was 2.1˚C higher than the reference white coating. While it was 23.3˚C lower than the reference black coating which showed the potential to be an effective NIR reflective pigment (Ianoș et al., 2017).

Figure 2.19

A Setup for an Indoor Cooling Effect Test. W, C, and B Indicated the Reference White Coating, the Pink Coating, and the Reference Black Coating, Respectively (Ianoș et al., 2017)

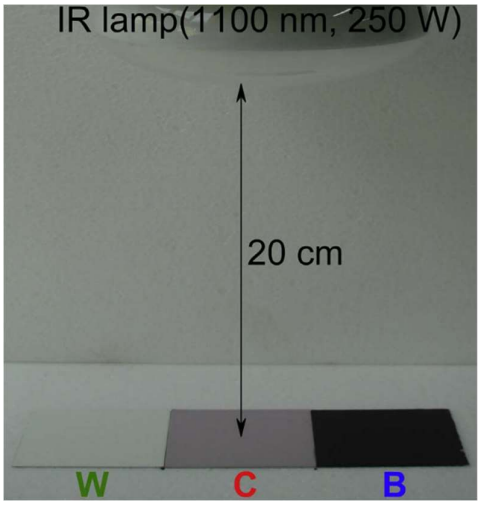

In another work by Ianoș et al., a combustion synthesis was utilized for the synthesis of a blue NIR reflective pigment with cobalt-doped zinc aluminate. The pigment was then mixed with water-based acrylic copolymer emulsion using a sinusdissolver with 30wt% of the pigment. The paint was coated on the 60mm×60mm aluminum sheet substrate using a block applicator with a 300 µm gap size. The TSR of the pigment was 63% and 59% for the coating. An indoor cooling effect test was conducted with an IR light bulb as a light source at a 20cm distance. A thermal camera FLIR T640 IR camera was used for temperature measurement with 15 frames/s. The reference materials are white and black coatings, similar to the previous work. The sample and reference coatings were exposed under the IR camera for 30 minutes. The temperature on the blue coating was 9˚C higher than the white coating and 16˚C lower than the black coating as shown in **Figure 2.20** *(Ianoş et al., 2017)*.

Figure 2.20

Surface Temperature Variation During IR Radiation Exposure and a Setup for an Indoor Cooling Effect Test. W, C, and B Indicated the Reference White Coating, the Blue Coating, and the Reference Black Coating, Respectively (Ianoş et al., 2017)

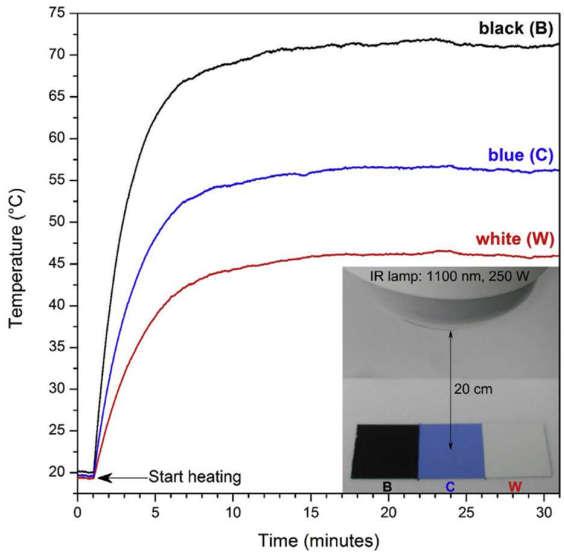

Brown NIR reflective pigment was synthesized with the mixture of Fe_2O_3 and Al_2O_3 via solid-state reaction. The pigment was then sprayed coating on the metal sheet after mixing with exterior paint with variations of percent weight of the pigment. The substrates were put under a 200W lamp for 5 hours and the temperatures on the surface and the opposite side of the substrate were measured. The highest temperature difference was 14˚C obtained from the pigment to exterior paint ratio of 30:70 (Busabok et al., 2018).

IR reflective and anti-dust polymer film was fabricated from the LDPE matrix mixed with black and brown commercial pigments. The pigments were blended using a HAAKE torque rheometer for 10 minutes at 130˚C with the variation of pigment content from 0-5wt%. The film was coated on the 20cm×15cm×2mm stainless steel plates. The NIR reflectance of 2wt% cool cold black pigment provided NIR reflectance up to 40%. An indoor cooling effect test was conducted under a 275W IR at a 40cm distance. A PS box, with 15cm×20cm×15cm dimensions and 2cm thickness, was used as an insulating system and the box was covered with the reflective film as shown in

Figure 2.21. The surface and inside temperatures were recorded with thermometers. The interior temperature under the cool cold black film was 15˚C lower than the reference carbon black film after 20 minutes of exposure (Zhang et al., 2018).

Figure 2.21

A Setup for an Indoor Cooling Effect Test (Zhang et al., 2018)

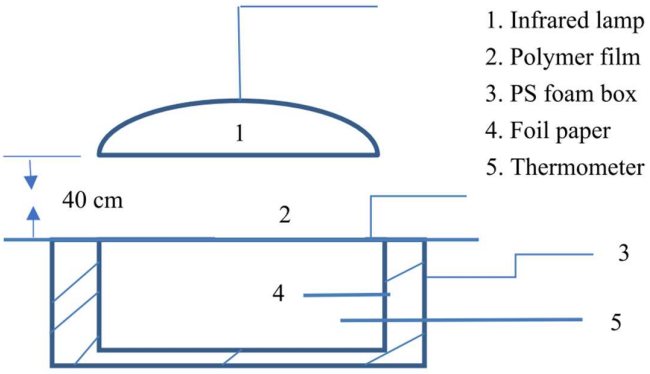

In Meenakshi et al., a bismuth titanate pale yellow IR reflective pigment was fabricated via the hydrothermal method. The pigment was mixed with B10 acrylic resin using mortar and pestle and painted on steel plates. The total solar A red IR lamp was used as a light source for the indoor cooling effect test which was 30cm away from the samples as shown in **Figure 2.22**. The temperatures at the front and back of the painted substrates were measured using thermocouples after 1 hour under the irradiation. Similar to the samples, TiO_2 reference coating underwent the same cooling effect test. The temperature difference on the front and back of the samples coated with yellow bismuth titanate was 10.2˚C while it was only 6.2˚C different on the TiO_2 reference as shown in **Figure 2.23** (Meenakshi & Selvaraj, 2018). TiO_2 is the material in commercial paint which is excellent in NIR reflective property. Accordingly, the bismuth titanate coating that can provide more temperature difference was a potential cool coating for surfaces.

Figure 2.22

An Experimental Setup for an Indoor Cooling Effect Test Under an IR Lamp Exposure (Meenakshi & Selvaraj, 2018)

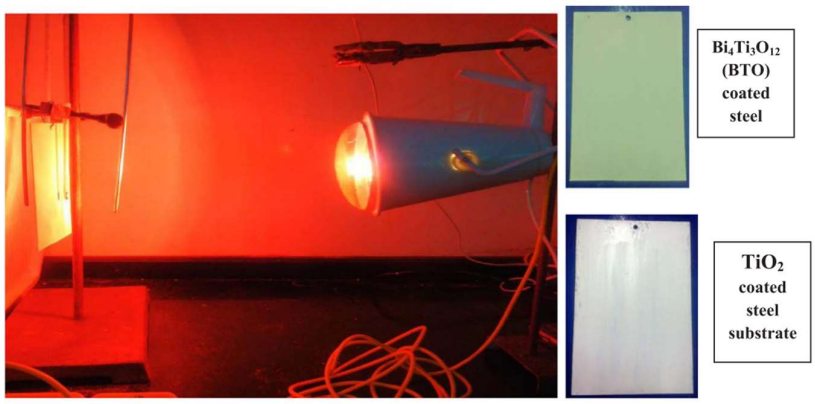

Figure 2.23

The Temperatures in Front and Behind the Substrates Painted With Bismuth Titanate Yellow NIR Reflective Pigment and Reference TiO_2 (Meenakshi & Selvaraj, 2018)

S.No	Sample	Thickness of coating (μm)	Temperature in front of panel (°C)	Temperature in behind the panel (°C)	Temperature difference (°C)
1.	BTO coated steel substrate	194	45.8	35.6	10.2
2.	TiO_2 coated steel substrate	198	50.6	44.4	6.2

Combustion synthesis was utilized in Ianoș et al. to synthesize a brown NIR reflective pigment from iron-doped lanthanum aluminate. The addition of iron was to add color to the pigment. However, the larger composition of the iron led to the lower TSR of the pigment. The coating was made from 20wt% pigment mixed with acrylic resin and coated on 60mm×60mm aluminum sheets by a block applicator with a 300μm gap size. The thickness of the thickness was around 91-101μm. The highest TSR of the synthesized pigment was 57.3% and 49.4% for the coating. The spectra was shown in **Figure 2.24**. For the cooling effect test, an IR lamp was set 20cm away from the coatings. The thermal images were recorded with FLIR T640 thermal camera with 15 frames/s for 35 minutes. The reference material was the lanthanum aluminate without iron doping. However, the temperatures on the iron-doped samples were higher than the undoped ones due to the lower TSR as shown in **Figure 2.25** (Ianoş et al., 2018).

Figure 2.24

Diffuse Reflectance Spectra and The Images of the Coatings With Various Compositions of the Iron Coatings (Ianoş et al., 2018)

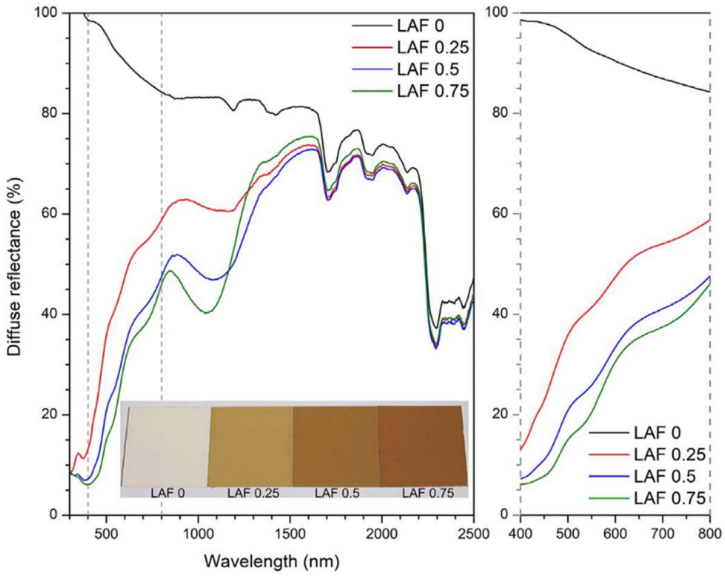

Figure 2.25

Recorded Temperatures From the Coating With Various Compositions of Iron Doping (Ianoş et al., 2018)

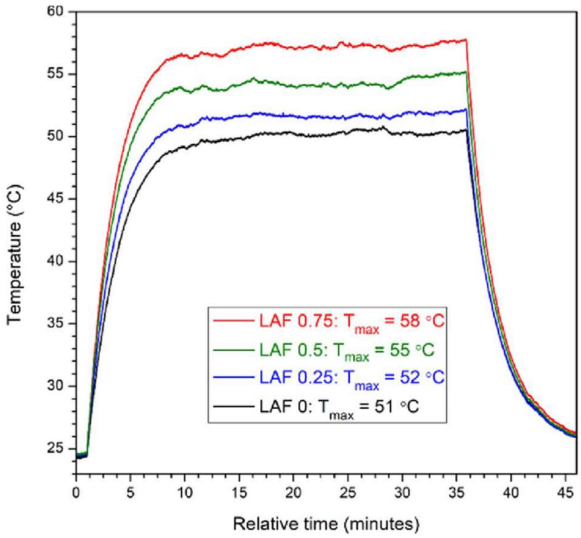

Yellow to deep yellow NIR reflective pigments were fabricated in Chen et al. using a high-temperature calcination method based on bismuth and yttrium mixed oxide doped with iron oxide and terbium oxide. The maximum NIR reflectances of the pigments were 87.02% and 99.87% for the iron oxide-doped and terbium oxide-doped pigments, respectively. The pigments were mixed with alkyd resin with a pigment to resin mass ratio of 1:1 and the coating was poured and self-slipped on 10cm×8cm galvanized sheets. For the indoor cooling effect test, the coated substrates were placed on heat insulating panels 25cm away from a 100W IR light source as shown in **Figure 2.26**. The surface temperatures were recorded with the IR thermal imager together with the iron oxide yellow pigment as a reference. The synthesized NIR reflective yellow pigment could provide a 5°C lower surface temperature than the reference after 10 minutes of the exposure (Chen et al., 2020).

Figure 2.26

Coated Samples and the Cooling Effect Test Under an IR Light Source (Chen et al., 2020)

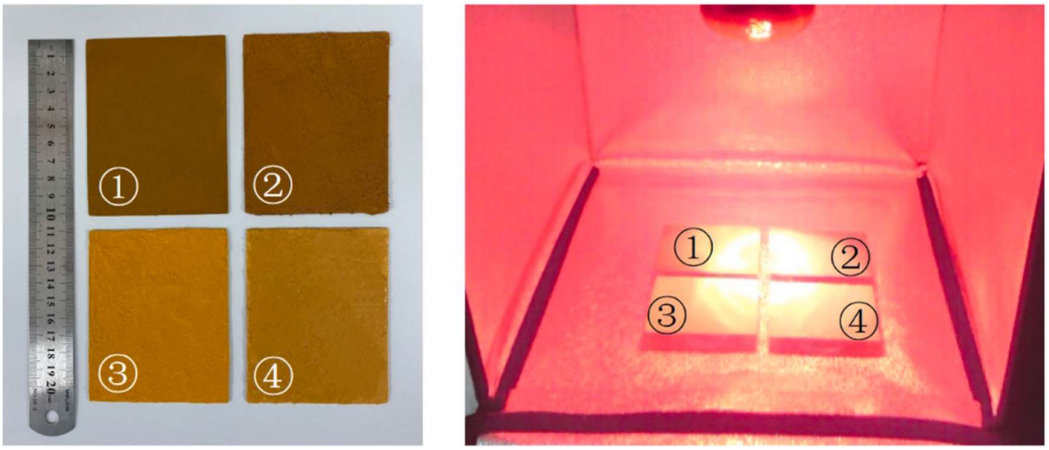

You et al. tested the commercial CuO macroparticle, CuO nanoparticles, and TiO_2 nanoparticles for the reflective coating on the asphalt pavement. The particles were mixed with epoxy resin with the pigment to resin ratio of 1:2, coated on the 20cm×20cm×5cm asphalt blocks with a plain brush, and cured at 23°C for 24 hours. The thickness was around 114-125μm. The TSRs of the coatings increased as the amount of the TiO_2 component increased. The T-type thermocouples and a logging

system were used for the outdoor cooling effect test under the sunlight for 7 days as shown in **Figure 2.27**. The reference for the coating effect test was the coating with the smallest amount of TiO_2. The temperature differences between the reference and the coatings with higher TiO_2 components were about 0.5-2.5°C (You et al., 2021).

Figure 2.27

A Schematic Diagram of the Outdoor Cooling Effect Test (You et al., 2021)

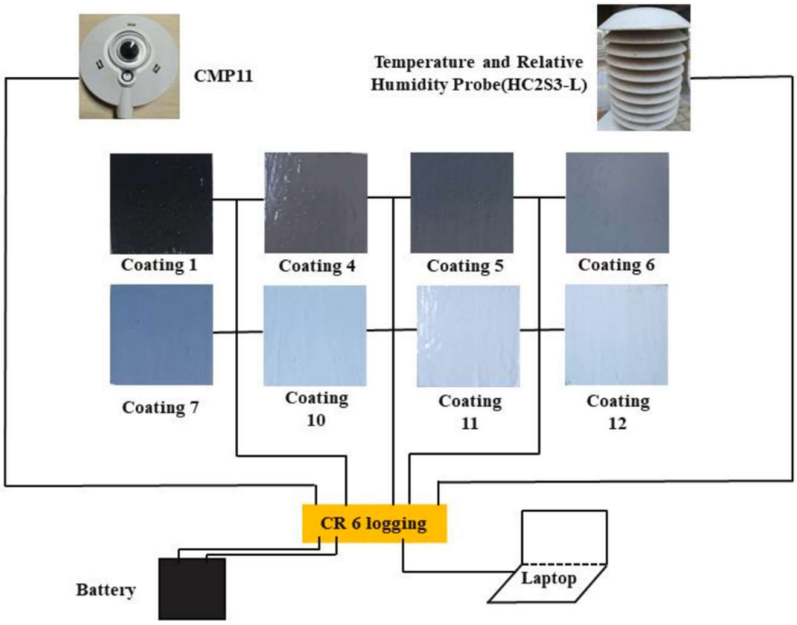

From the mentioned works above, some coating preparations and setups were summarized in **Table 2.3** for the cooling effect test overview.

Table 2.3

The Table Summarizes the Cooling Effect Tests in Several Studies of Cooling Coatings

Source	Color	Matrix	Amount of pigment	Setup	The reflectance of the pigment		The reflectance of the coating		Light source	Distance from the light source	Time of exposure	Thermometer	Temperature difference (from the reference)
					TSR	NIR	TSR	NIR					
(Thongkanluang et al., 2011)	Green	-	-	Gypsum boards built into roofs for house models	-	82.8%	-		The sun	-	4 days	K-type thermocouples and a data logger	1.3-2.5 °C
(Xiang et al., 2015)	Green	HDPE	-	Compressed HDPE on a thermally insulated cylinder	-		16.2%	-	The sun	-	1h	Mercury thermometer	5°C
(Qi et al., 2017)	White	ASA resin	-	Compressed ASA on a thermally insulated cylinder	-		70.9%	63%	The sun	-	1h	Mercury thermometer	5-10°C
(Ianoş et al., 2017)	Pink	Water-based acrylic	20wt%	Aluminum sheets on a white PS board	69.2%	-	61.7%	-	250W IR lamp	20cm	30min	FLIR T640 IR camera with 15 frames/s	23.3°C
(Ianoş et al., 2017)	Blue	Water-based acrylic copolymer -emulsion	30wt%	Aluminum sheets on a white PS board	63%	-	59%	-	250W IR lamp	20cm	30min	FLIR T640 IR camera with 15 frames/s	16°C
(Zhang et al., 2018)	Black	LDPE	5wt%	Stainless steel substrate on a PS box	-		-	40%	275W IR lamp	-	20min	Thermometers	15°C
(Chen et al., 2020)	Yellow	Alkyd resin	1:1 pigment:resin	Galvanized sheets	-	99.87%	-		100W IR lamp	25cm	10min	IR thermal camera	5°C

2.6 Chapter Summary

This chapter reviews the causes and impacts of the heat island effect which affect three main aspects of human health and well-being, the economy, and the environment. Moreover, the countermeasures to the heat island effect were also studied. The mitigations could be in the forms of the appropriate city design, addition of green infrastructures, utilization of NIR reflective infrastructures, and effective policies. NIR reflective coating is an effective way to mitigate the heat island effect and the NIR reflective pigments can be fabricated with several methods including solid-state, precipitation, hydrothermal, and sol-gel synthesis. The sol-gel approach is a simple, low-cost, and energy-efficient method such that the technique was selected for this project.

With the synergy of the core-shell nanostructure, the pigment can provide both color and NIR reflectivity to the coatings where Al_2O_3, Fe_2O_3, and Cr_2O_3 are three core materials for this work due to their availability and non-toxicity. Therefore, this chapter contains the literature review of the sol-gel synthesis of Al_2O_3-TiO_2, Fe_2O_3-TiO_2, and Cr_2O_3-TiO_2 core-shell nanoparticles where the sol-gel synthesis of the Cr_2O_3-TiO_2 core-shell nanoparticles can be rarely found. Accordingly, the cooling property evaluation is an important part of this work. The cooling effect tests, both indoor and outdoor, were reviewed and summarized for the references of this work.

CHAPTER 3
METHODOLOGY

3.1 Overall Methodology

The methodology started with the synthesis of core-shell nanoparticles which is the simple sol-gel synthesis. After the synthesized particles were obtained, the particles underwent DLS, TEM, SEM, and XRD characterizations to observe the size, structure, morphology, crystalline phase, and most importantly, the NIR reflectance investigation. After the required particles were obtained, the pigments were prepared into coatings for the cooling effect evaluation.

The main materials were the metal oxides of Al_2O_3, Fe_2O_3, and Cr_2O_3. The titanium source was the TTIP. Other main chemicals were EtOH, tween 80, and DI water.

Figure 3.1

A Flow Chart Shows the Overall Methodology of This Work

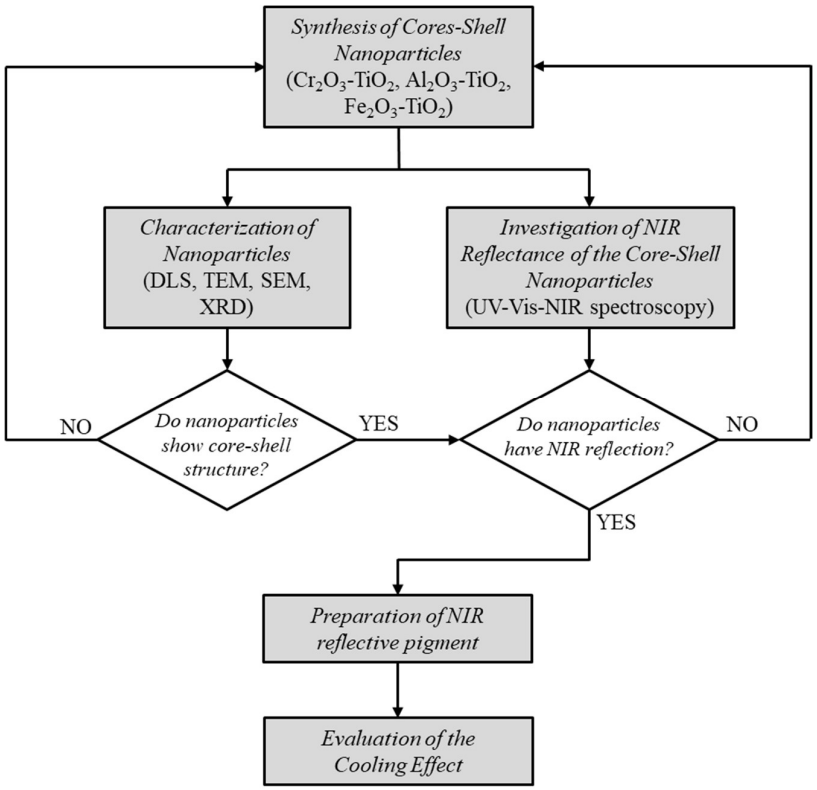

3.2 Sol-Gel Synthesis of Core-Shell Nanoparticles

Adapted from Karunakaran et al. (Karunakaran et al., 2015), to synthesize the metal oxides-TiO_2 core-shell nanoparticles using the sol-gel method, 0.06g of metal oxides nanoparticles were suspended in 2ml of DI water for 10 minutes using a magnetic stirrer. Then the suspensions were dried in an oven at 80°C for 1 hour or until almost dried. The metal oxide core was redispersed in 50ml of ethanol via the magnetic stirrer for 5 minutes and via an ultrasonic probe sonicator for 20 minutes to obtain a homogenous mixture. DI water was added for the initialization of the hydrolysis reaction. 2ml of tween 80 was added to the mixture to improve the dispersion of the metal oxide core in ethanol and stirred for 30 minutes. To this mixture, 3, 4, and 5ml of titanium isopropoxide was dropwise added and continuously stirred for 3, 6, and 10 hours. The solution was then aged for at least 3 hours for the precipitation of the pigment. The precipitated gel was collected into the porcelain crucible. The gel is dried at 100°C for 6 hours in an oven and calcined at 500°C for 3 hours in a muffle furnace with a heating rate of 5°C/min to obtain the anatase TiO_2 shell. The samples were then weighted, ground, and collected. The overall process is shown in **Figure 3.2**. The samples synthesized with different conditions were named as follows. The first two letters, Al, Fe, or Cr, in sample codes, indicate the metal oxide cores of Al_2O_3, Fe_2O_3, and Cr_2O_3, respectively. The third and fourth positions, 03, 06, and 10, are the gelation time of the sample followed by the volume of TTIP and gelation temperature used in the synthesis. For example, Al063 is the Al_2O_3-TiO_2 core-shell nanoparticles fabricated with 6 hours of gelation and 3ml of TTIP at RT. Fe03340 is the Fe_2O_3-TiO_2 core-shell nanoparticles fabricated with 3 hours of gelation and 3ml of TTIP at 40°C.

Figure 3.2

A Schematic Diagram Shows the Overall Synthesis Protocol of the Al_2O_3-TiO_2, Fe_2O_3-TiO_2, and Cr_2O_3-TiO_2 Core-Shell Nanoparticles

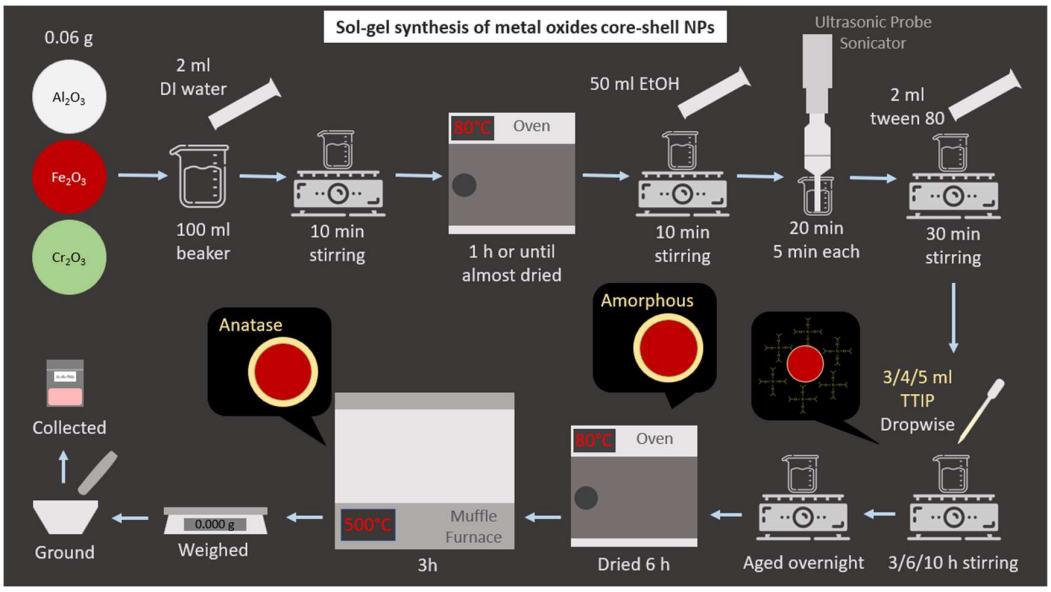

3.3 Characterization of Nanoparticles

The particle size of the metallic cores and the synthesized pigments was investigated with Malvern ZETASIZER NANO ZS laser diffraction particle size analysis. The obtained information can be the primary, aggregated, and agglomerated size of the particles. Primary size is the size of an individual particle. However, due to the high surface-to-volume ratio of the particles, particles tend to agglomerate together to reduce their surface energy and when the samples are calcined, the particles were aggregated together with a strong bonding that cannot be broken with mechanical forces. On the other hand, agglomeration is just a weak bonding that can be destroyed easily (Ashraf et al., 2018).

For SEM characterization, a small amount of pigment was dispersed in ethanol to obtain a diluted solution, dropped on an SEM stub, and dried in the air. The solution must be diluted since concentrated solution leads to agglomeration of the samples which causes a charging effect leading to a blur SEM image. SEM characterization was performed to observe the size and morphology of the commercial metallic cores and synthesized

nanoparticles. Moreover, EDS was performed along with SEM to identify the elements present in the samples. The SEM model was JSM-7800FPRIME Schottky FESEM with 10kV. The SEM images were taken at 20x magnification to see the overall morphology and at 40x to see the details.

For TEM sample preparations on carbon-coated copper grids, diluted solutions were prepared in 1ml Eppendorfs by dispersing a very small amount of the pigment in 1ml of DI water. The Eppendorfs were sonicated for 40 minutes using 70% power with 53kHz. A glass slide was cleaned with acetone and placed on a Petri dish. The carbon-coated copper grids were placed on the glass slide with the carbon-coated side (not the shiny side) upward. The dispersed samples were dropped on copper grids via a micropipette. Forceps were used for holding the edges of the grids preventing them from floating. The Petri dish was closed and left to stand for 30 minutes. Water droplets were removed and the grids were pushed by filter papers to the edge of the glass slide. The grids were transferred via forceps to another cleaned glass slide stuck on another Petri dish. The Petri dish was closed and placed in an incubator for 2 hours to let the grids dry. The grids were transferred into a grid storage box and kept in the incubator before sending to TEM characterization.

TEM images at a 10,000 to 20,000x magnification range were captured to observe the overall picture of the synthesized pigments. At 50,000x magnification, the image shows the structure of an individual nanoparticle or a small cluster of nanoparticles. In the range of 100,000 to 600,000x magnification, the images provide more details of the structures on the surface. In addition, the selected area diffraction pattern (SAED) was captured to determine the crystal orientation and lattice constants of the samples.

Rigaku TTRAX III XRD was used for determining the crystalline phases of the synthesized nanoparticles. The 2θ range was 10-90° with a scan speed of 3°/min (0.02 sampling width, 50kV power, and 300mA current). The relative ratio of the crystalline phases and the crystallite size can be roughly calculated using the open-source Profex software. For XRD sample preparation, a spatula was used for spreading pigments to cover all the area on a glass sample holder. The surface of pigments was smoothened by a glass substrate and the excess powder was removed from the holder.

3.4 Investigation of NIR Reflectance of the Core-Shell Nanoparticles

The NIR reflectance of the core-shell nanoparticles was investigated by using Shimadzu's SolidSpec-3700i spectrophotometer. The Total Solar Reflectance (TSR) and NIR solar reflectances (R) in the wavelength range of 300-2500nm and 700−2500nm, respectively, were measured and calculated with ASTM Standard No. E903-96 and calculated using the computation of E891BN solar reflectance. The reflectance of the samples was measured every 5nm per step. From 300 to 2500nm, the reflectance reflected by a surface is the irradiance-weighted average of its spectral reflectance, r(λ), which can be determined using **Equation 3.1.**

$$R^* = \frac{\int_{300}^{2500} r(\lambda) i(\lambda) d(\lambda)}{\int_{300}^{2500} i(\lambda) d(\lambda)} \qquad (3.1)$$

Where $r(\lambda)$ is the experimentally obtained spectral reflectance (Wm^{-2}), and $i(\lambda)$ is the solar spectral irradiance ($Wm^{-2}\,nm^{-1}$) obtained from the ASTM Standard No. E903-96 and calculated using the computation of E891BN solar reflectance.

3.5 Preparation of NIR Reflective Pigments

In a beaker, 1g of the grounded pigments were stirred in 1.5g water-based acrylic base (white color) with a metallic spatula until a homogeneous mixture was obtained to get 40%wt of the pigment. The screen-printing frame was laid on an aluminum substrate. The mixture was then poured onto the screen-printing frame and coated on the aluminum substrate with a squeegee as shown in **Figure 3.3**. The coatings were allowed to dry in the air which took around 10 minutes and repeat the coating process to make sure that the surface was fully covered.

Figure 3.3

Coating Preparation for the Cooling Effect Evaluation

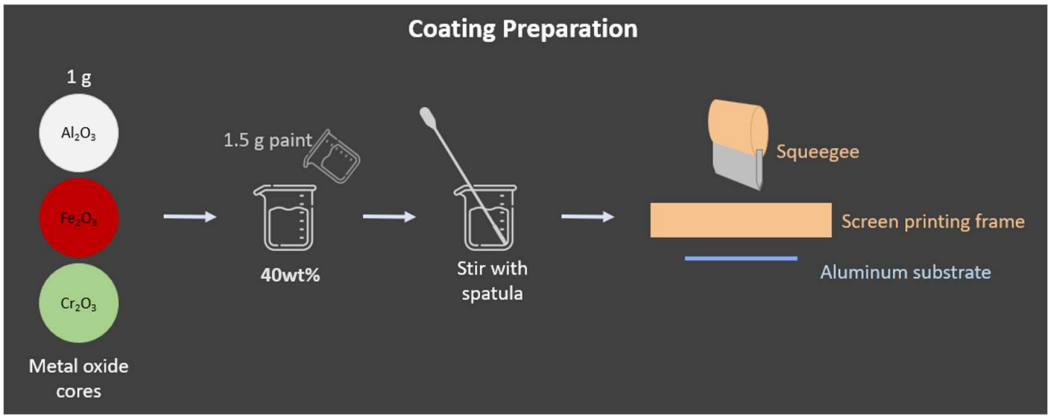

To evaluate the efficiency of the NIR-reflective pigment, a similar paint without NIR reflectivity was prepared using core materials, Al_2O_3, Fe_2O_3, and Cr_2O_3, with the same amount as the NIR reflective pigments.

3.6 Evaluation of the Cooling Effect

A Polystyrene (PS) foam box was used as a thermal insulating chamber. The lid was punched as the same size as the aluminum substrate such that the temperature inside was not affected by environmental factors. The coated substrate was then placed to cover the hole. The temperature on the coated substrate was monitored and noted every 5 minutes for the interval of 2 hours via a thermal camera for the cooling effect evaluation when placed under NIR light bulb. The temperature was double-checked via a thermocouple attached to the surface. Moreover, the temperatures under the substrate, in the middle of the box, and outside the box were also observed using thermocouples as shown in **Figure 3.4** and the set-up was shown in **Figure 3.5**. A Lutron TM-1947SD thermometer was used as a data logger with type K thermocouples. Other substrates were prepared coating with the Al_2O_3, Fe_2O_3, and Cr_2O_3 metallic core materials as control samples, and the cooling effect was evaluated similarly. The cooling effect was considered from the temperature difference between the control sample and the NIR reflective coated enclosure.

Figure 3.4

A Graphic Shows the Insulative Box Used in the Cooling Effect Evaluation and the Positions of the Thermocouples

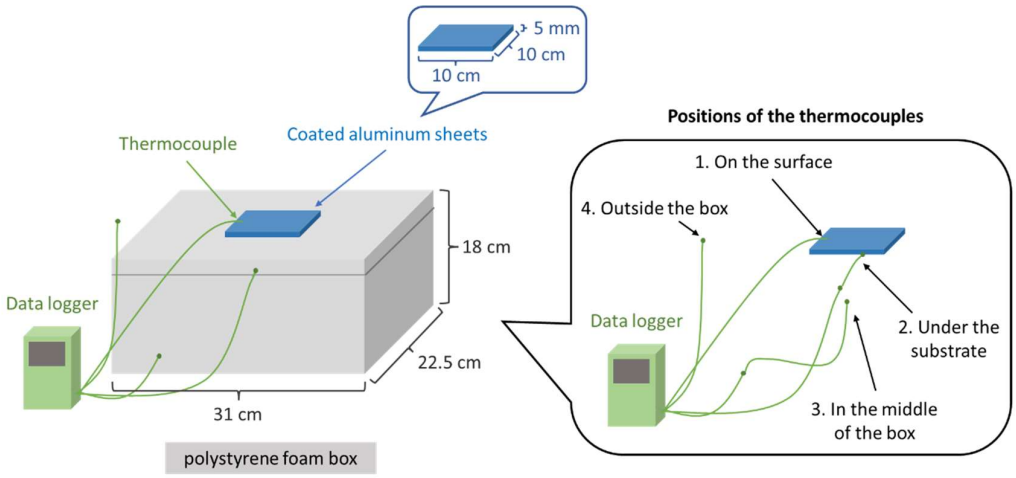

Figure 3.5

A Graphic and Practical Setup of the Indoor Cooling Effect Evaluation Under NIR Irradiation

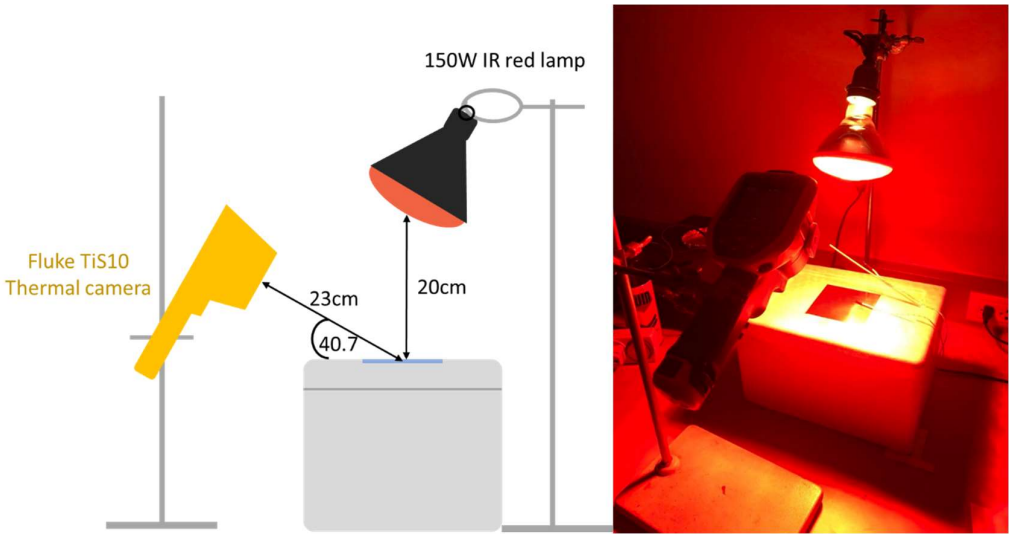

CHAPTER 4
RESULT & DISCUSSION

4.1 SEM Characterizations

SEM images of both metal oxide cores and the synthesized particles were captured at 40kX magnification as shown in **Figure 4.1**, **Figure 4.2**, and **Figure 4.3**. Al063, Al064, Al103, Fe063, Fe064, Fe103, Cr063, Cr064, and Cr103 are the samples selected for the SEM characterization to observe any trend in the increase of TTIP volume and the gelation time. The surface of the metal oxide cores was smooth and the shape of the particles was polygon. On the other hand, the synthesized particles have a round structure and a rough surface. The synthesized pigments also have a larger size than the pure metal oxide cores. However, there is no obvious trend in the increase of TTIP volume and gelation time.

Figure 4.1

SEM Images of Al063 (a.), Al103 (b.), Al064 (c.), and Al_2O_3 Metal Oxide (d.)

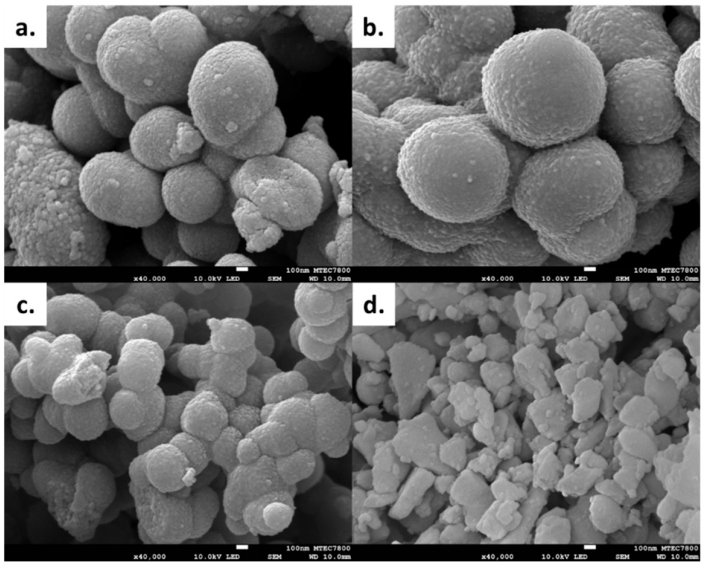

Figure 4.2

SEM Images of Fe063 (a.), Fe103 (b.), Fe064 (c.), and Fe_2O_3 Metal Oxide (d.)

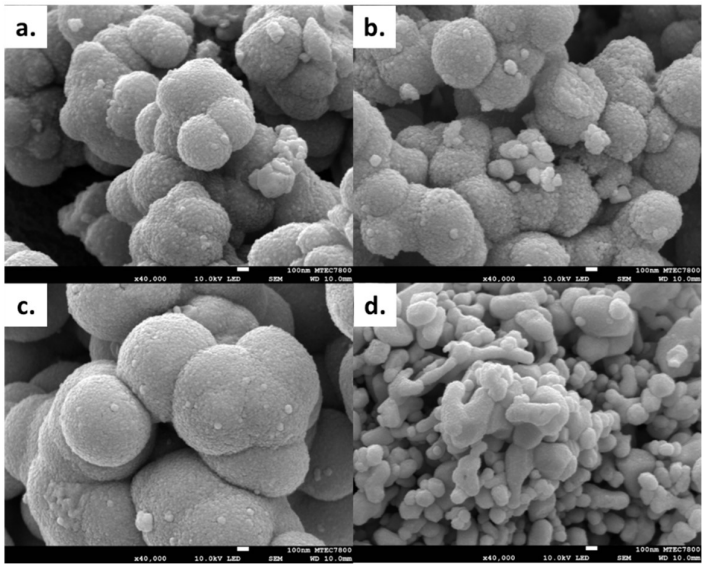

Figure 4.3

SEM Images of Cr063 (a.), Cr103 (b.), Cr064 (c.), and Cr_2O_3 Metal Oxide (d.)

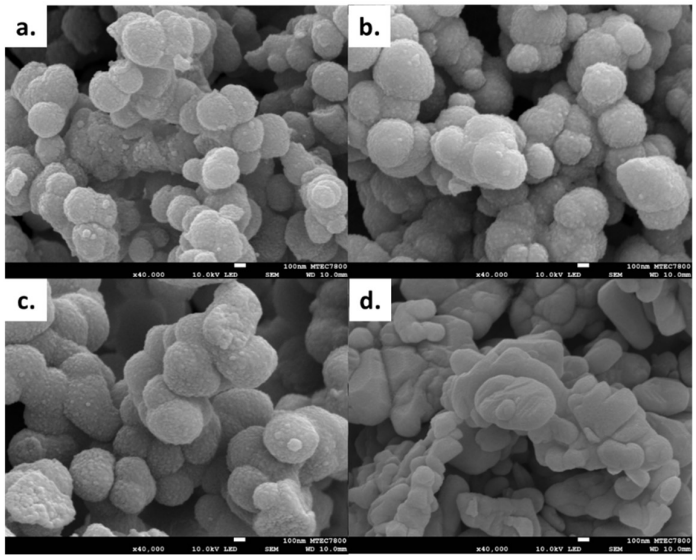

To confirm the elements of the samples and the trace of the core-shell structure, EDS and elemental mapping were performed along with the SEM characterization as shown

in **Figure 4.4**, **Figure 4.5**, and **Figure 4.6**. For synthesized particles, the EDS results show the high intensity of Ti compared to the metal Al, Fe, and Cr. The reason could be that the main element on the surface is Ti which indicated that the metal oxide cores were covered with TiO_2. In addition, the elemental mapping results offer a high density of Ti and O compared to metal oxide cores (Karunakaran et al., 2015; Yang et al., 2019; Zhang et al., 2014). In **Figure 4.6** (c.), a high density of Cr can be observed which might be the trace of thin TiO_2 which covered the Cr_2O_3. However, the empty space in SEM images provided some signal in the elemental mapping, which could be the background signal or noise from the sample. Therefore, it cannot be confirmed from the EDS results that the particles have core-shell structure.

Figure 4.4

SEM (a.)-EDS (b.)-Elemental Mapping (c.) Images of Synthesized Al063 Al_2O_3-TiO_2 Particles

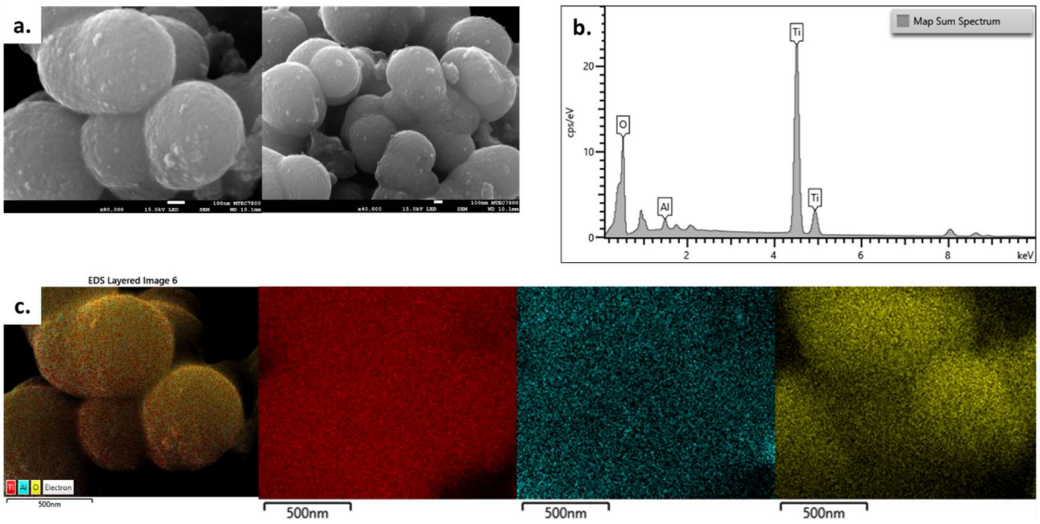

Figure 4.5

SEM (a.)-EDS (b.)-Elemental Mapping (c.) Images of Synthesized Fe063 Fe_2O_3-TiO_2 Particles

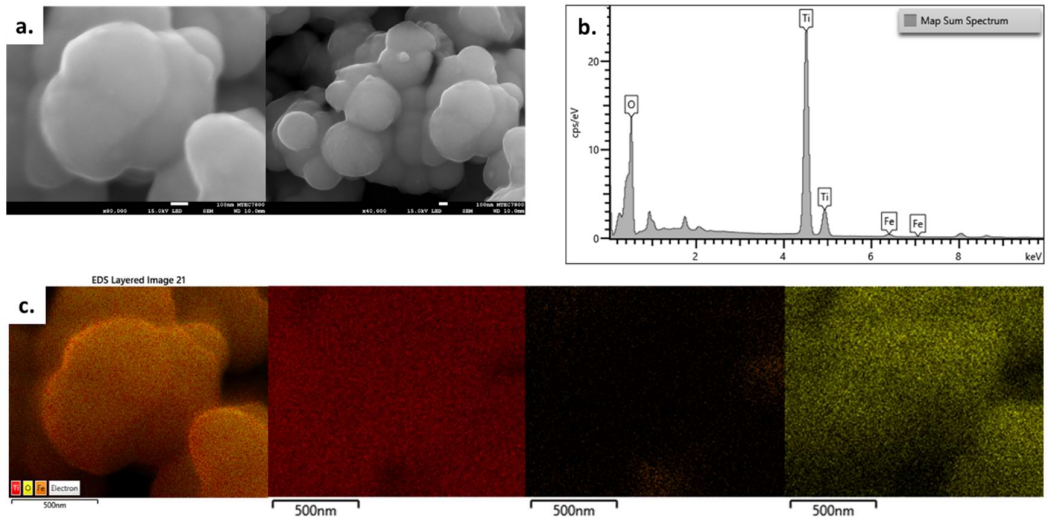

Figure 4.6

SEM (a.)-EDS (b.)-Elemental Mapping (c.) Images of Synthesized Cr063 Cr_2O_3-TiO_2 Particles

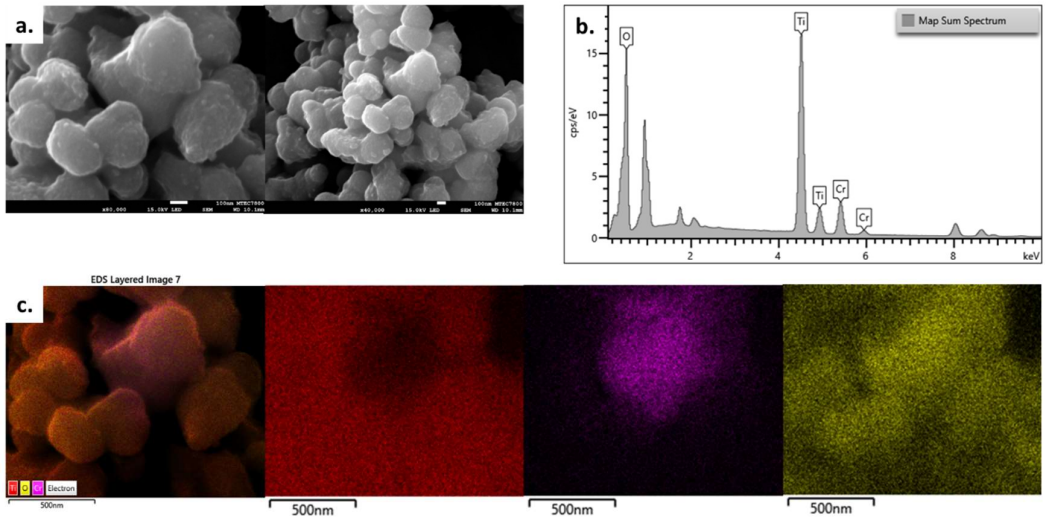

4.2 TEM Characterizations

To investigate the core-shell structure of the synthesized pigments, TEM images of Al063 and Al064 were demonstrated in **Figure 4.7**. TEM images of Fe063 and Fe103 were demonstrated in **Figure 4.8**. TEM image of Cr064 was demonstrated in **Figure 4.9**. The low magnification images showed that the particles tend to agglomerate together. The images showed the possibility of the core-shell structures as the darker part could be the higher density metallic cores and the light part could be the lower density TiO_2 shell.

The 600kX magnification images showed the crystal planes which reveal the polycrystallinity of the shell part. Therefore, the rough surface in SEM images was expected to be the polycrystalline TiO_2. In **Figure 4.8**, a large smooth surface particle was expected to be an Fe_2O_3 particle that was not covered with the TiO_2 as indicated by the red arrow. **Figure 4.9** revealed the polygon shape particle covered with a polycrystalline shell which was expected to be a Cr_2O_3 particle covered with a thin layer of TiO_2 shell. Moreover, the dark field image as shown in **Figure 4.10** (b.) exhibited the highly crystalline part in a bright contrast which confirmed that the polygon particle was a metal oxide core. This indicates that some particles have core-shell structure and some are just the TiO_2 particles alone.

Figure 4.7

TEM Images of Al064 at 500X (a.), 20kX (B.), and 50kX (C.) Magnifications, and Al063 at 600kX Showing the Overall and Individual Image of the Particles and Also the Polycrystalline Structures on the Shell Part

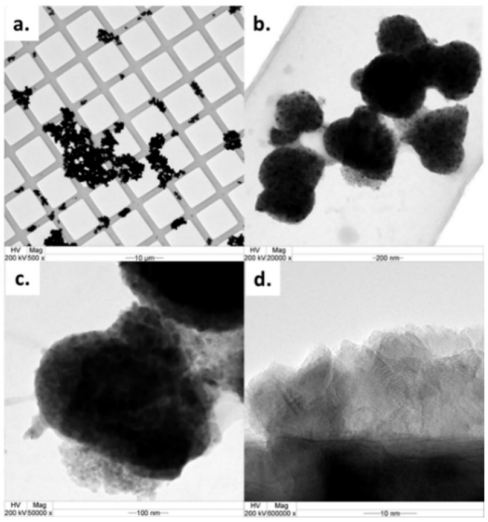

Figure 4.8

TEM Images of Fe103 at 10kX (a.) and 20kX (B.) Magnifications and Fe063 100kX (C.) and 600kX (D.) Magnifications Showing the Overall and Individual Image of the Particles and Also the Polycrystalline Structures on the Shell Part

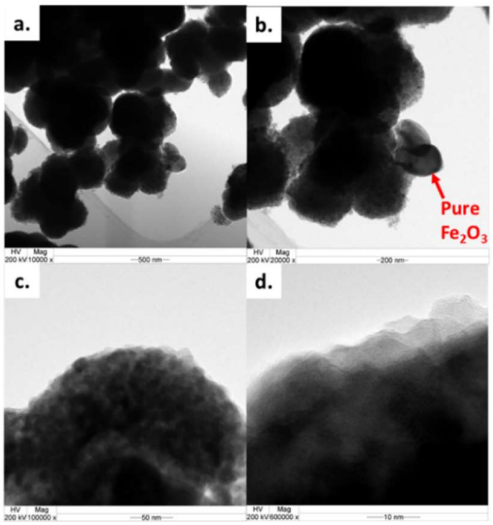

Figure 4.9

TEM Images of Cr064 at 10kX, 50kX, 100kX, and 600kX Magnifications Showing the Overall and Individual Image of the Particles and Also the Polycrystalline Structures on the Shell Part

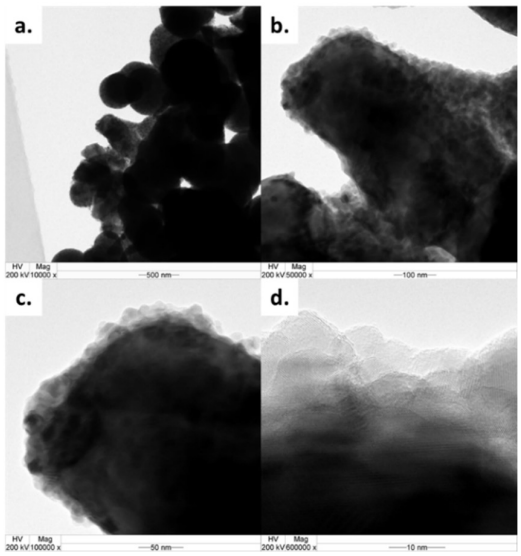

Figure 4.10

Bright (a.) and Dark-field (B.) TEM Images of Cr064 at 10kX Magnification Showing High Crystallinity Structures of Cr_2O_3 Hidden in the Synthesized Particles

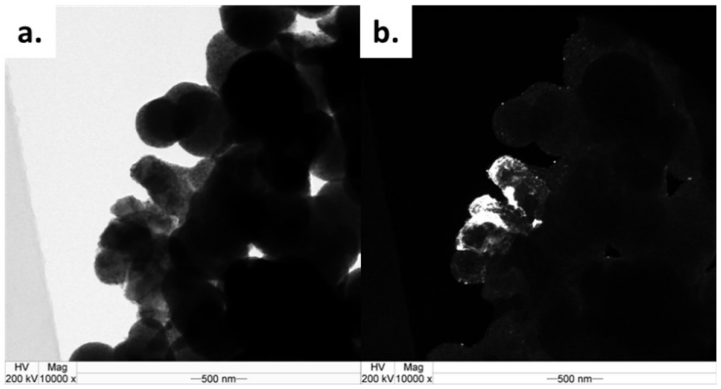

Moreover, TEM-EDS-SAED results were captured to confirm the elements of the synthesized particles as shown in **Figure 4.11**, **Figure 4.12**, and **Figure 4.13** for Al063, Fe063, and Cr064 accordingly. The EDS results confirmed the presence of Al, Fe, Cr, Ti, and O which are the composition of the Al_2O_3, Fe_2O_3, and Cr_2O_3 metal oxides and TiO_2. The SAED patterns show the array of dots of highly crystalline metal oxides and continuous rings of polycrystalline TiO_2. Apparently, in **Figure 4.13**, the EDS result (c.) shows a significantly high intensity of Cr and the SAED pattern (d.) reveals bright arrays of dots which confirmed the presence of Cr. In addition, the polygon structure wrapped with a polycrystalline shell can be seen in the TEM images in **Figure 4.13** (a., b.). The thin shell makes the EDS signal of Cr in **Figure 4.13** (b.) higher than Al and Fe in **Figure 4.11** (b.) and **Figure 4.12** (b.).

Figure 4.11

TEM Images (a.), EDS (b.), and SAED (c.) Pattern of Al063 Showing the Presence of Single Crystalline Al_2O_3 and Polycrystalline TiO_2

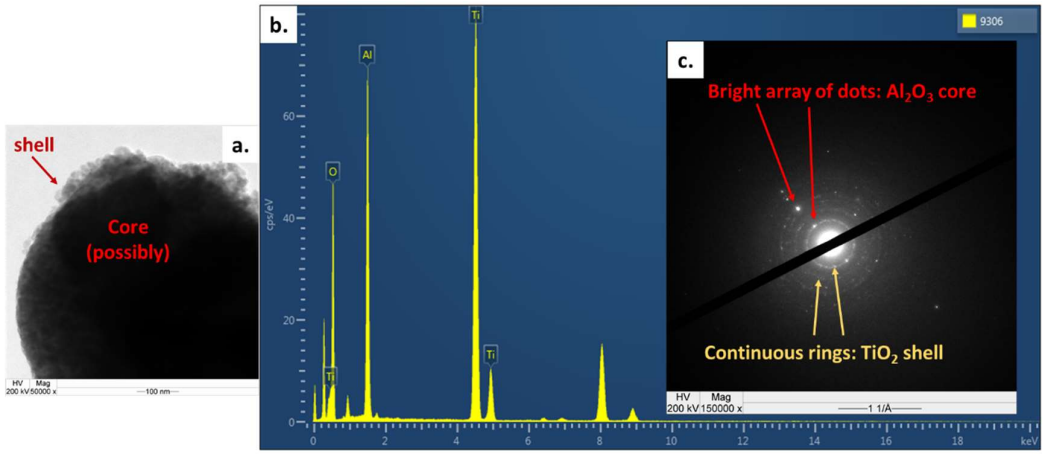

Figure 4.12

TEM Images (a.), EDS (b.), and SAED (c.) Pattern of Fe063 Showing the Presence of Single Crystalline Fe_2O_3 and Polycrystalline TiO_2

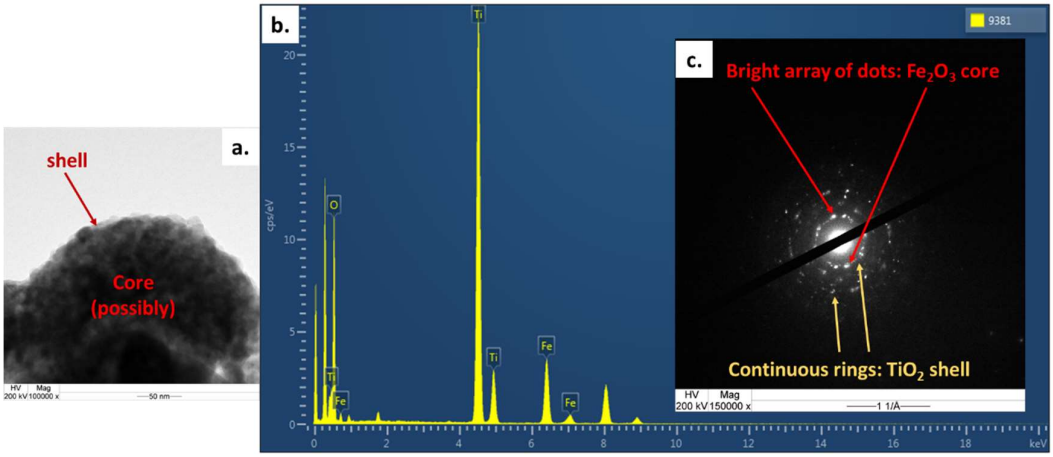

Figure 4.13

TEM Images (a.), EDS (b.), and SAED (c.) Pattern of Cr064 Showing the Presence of Single Crystalline Al_2O_3 and Polycrystalline TiO_2

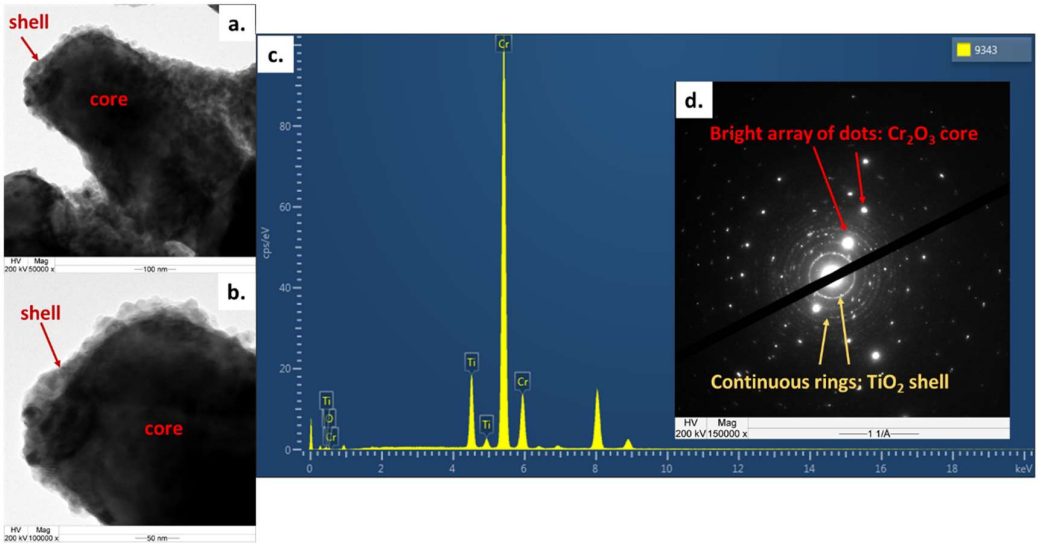

4.3 Particle Size Analysis

Particle size obtained from laser diffraction particle size analysis can be the primary, aggregated, and agglomerated size of the particles. Primary size is the size of an individual particle. However, due to the high surface-to-volume ratio of the particles, particles tend to agglomerate together to reduce their surface energy and when the samples are calcined, the particles were aggregated together with a strong bonding that cannot be broken with mechanical forces. On the other hand, agglomeration is just a weak bonding that can be destroyed easily (Ashraf et al., 2018). Therefore, the particle size obtained could be larger than the individual particle.

The particle size of the metal oxides and the synthesized samples were demonstrated in **Table 4.1**, **Table 4.2**, and **Table 4.3** for Al_2O_3-TiO_2, Fe_2O_3-TiO_2, and Cr_2O_3-TiO_2 accordingly. It could be noticed that the size of the synthesized particles significantly increased from the size of the metal oxide cores and increased as the gelation time was extended from 3 to 6 hours. However, from 6 to 10 hours of gelation, the size was comparable. This could lead to the conclusion that 6 hours are enough to complete the gelation of TiO_2.

In terms of the TTIP volume and gelation temperature, there is no obvious trend that the size would change along with the increase of these parameters which might need further repetition to confirm the results.

Table 4.1

Size of the Al_2O_3 and Al_2O_3-TiO_2 Synthesized With Different Conditions

Size of Al_2O_3 and Al_2O_3-TiO_2 (µm)					
TTIP (ml)	Gelation Time (hours)				
	3			6	10
	RT	40°C	60°C	RT	RT
Pure Al_2O_3	0.79	-	-	-	-
3	8.54	10.89	6.56	7.33	11.45
4	1.75	-	-	5.55	6.85
5	4.18	-	-	6.2	6.16

Table 4.2

Size of the Fe_2O_3 and Fe_2O_3-TiO_2 Synthesized With Different Conditions

Size of Fe_2O_3 and Fe_2O_3-TiO_2 (µm)					
TTIP (ml)	Gelation Time (hours)				
		3		6	10
	RT	40°C	60°C	RT	RT
Pure Fe_2O_3	3.02	-	-	-	-
3	6.28	3.69	3.05	9.57	13.39
4	4.89	-	-	16.53	11.57
5	5.81	-	-	12.54	10.78

Table 4.3

Size of the Cr_2O_3 and Cr_2O_3-TiO_2 Synthesized With Different Conditions

Size of Cr_2O_3 and Cr_2O_3-TiO_2 (µm)					
TTIP (ml)	Gelation Time (hours)				
		3		6	10
	RT	40°C	60°C	RT	RT
Pure Cr_2O_3	2.94	-	-	-	-
3	4.33	5.67	7.76	17.16	6.43
4	8.74	-	-	13.66	12.93
5	9.42	-	-	7.48	22.63

4.4 X-Ray Diffraction

XRD patterns were obtained to observe the crystal phase of Al033, Fe104, and Cr065 compared to metal oxides and TiO_2. The phase composition and crystallite size were calculated via Profex software (Doebelin & Kleeberg, 2015).

In Al033, the relative phase quantities of anatase TiO_2 and corundum Al_2O_3 were 88.15 and 11.85% with the crystallite size of 25 and 105 nm. The XRD pattern of Al033 can be observed in **Figure 4.14**. The stronger peak might indicate the larger amount of TiO_2 presence on the surface over Al_2O_3 which could be the trace of core-shell structure.

Figure 4.14

XRD Patterns of the Al033 Compared to Pure TiO_2 and Al_2O_3

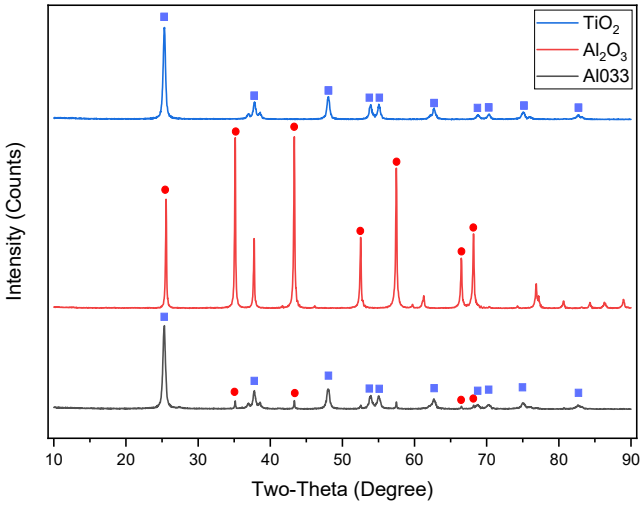

Figure 4.15 showed the XRD pattern of Fe104 corresponding with relative phase quantities of 94.84% and 5.16% for anatase TiO_2 and hematite Fe_2O_3 where the crystallite sizes were 19.4 and 499 nm, accordingly. Similarly to Al033, the pattern showed stronger peaks of TiO_2 than the Fe_2O_3.

Figure 4.15

XRD Patterns of the Fe104 Compared to Pure TiO_2 and Fe_2O_3

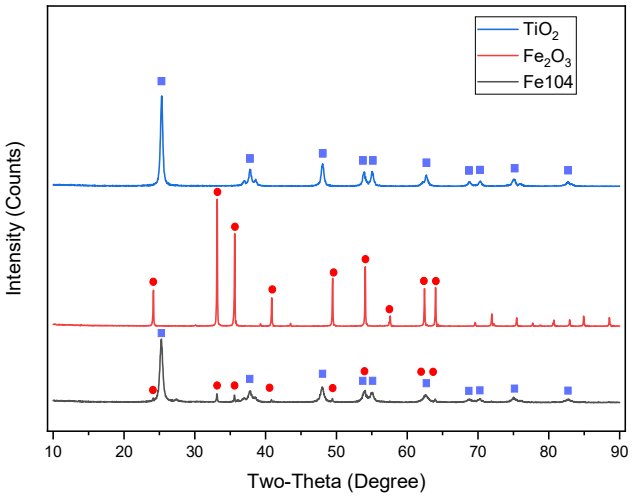

For Cr065, the relative phase quantities of anatase TiO_2 and Cr_2O_3 were 96.42 and 3.58% with the crystallite size of 21.1 nm for TiO_2. However, the crystallite size of Cr_2O_3 was not identified. The corresponding XRD pattern, **Figure 4.16**, provided a similar result to Al033 and Fe104 which could be the trace of core-shell structures.

Figure 4.16

XRD Patterns of the Cr065 Compared to Pure TiO_2 and Cr_2O_3

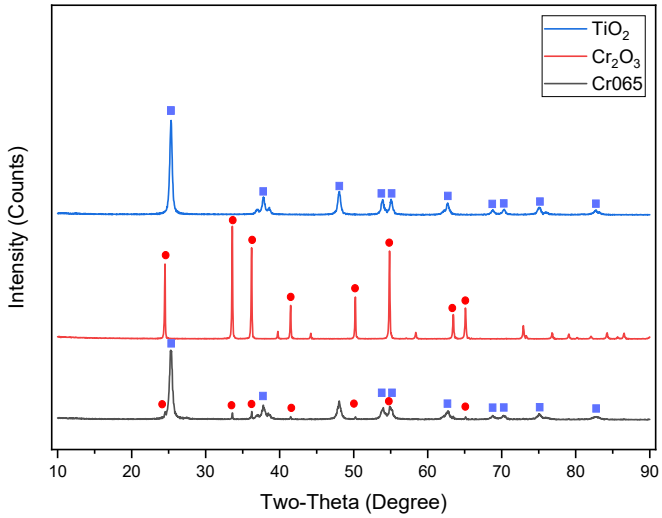

Therefore, these XRD results confirmed the elemental composition and crystalline phase of the Al_2O_3-TiO_2, Fe_2O_3-TiO_2, and Cr_2O_3-TiO_2. Moreover, the stronger peaks of TiO_2 might indicate that the metal oxide cores were covered with the TiO_2 shell (see Appendix for raw data).

4.5 Total Solar and NIR Reflectance

4.5.1 Powder Samples

TSR and NIR reflectance is the important characteristic of the NIR reflective pigments. The reflectivity of the metal oxide cores, synthesized pigments, and TiO_2 was compared to observe any improvement after coating the metal oxides with TiO_2 and to observe any trend in the increase of gelation temperature, gelation time, and TTIP volume.

Al_2O_3 originally has high TSR and NIR reflectance up to 97.5 and 96.9% such that the enhancement of the core-shell structure cannot be seen obviously as listed in **Table 4.4**.

However, both TSR and NIR reflectance of the synthesized particles was considered high and comparable to TiO_2 which is the common material found in white paint. Especially, Al033 which provided the highest TSR and NIR reflectance up to 95.3 and 98.6%, respectively.

Table 4.4

TSR and NIR Reflectance of the Al_2O_3-TiO_2 Synthesized With Different Conditions Compared to Pure TiO_2 and Al_2O_3

Reflectance (%R)						
TTIP (ml)		Gelation Time (hours)				
			3		6	10
		RT	40°C	60°C	RT	RT
Al_2O_3	TSR	97.5	-	-	-	-
	NIR	96.9	-	-	-	-
TiO_2	TSR	98.2	-	-	-	-
	NIR	100.3	-	-	-	-
3	TSR	95.3	91.9	93.2	85.2	85.9
	NIR	98.6	95.9	96.7	91.6	92.3
4	TSR	94.5	-	-	94.5	91.2
	NIR	97.6	-	-	98.3	95.6
5	TSR	93.6	-	-	93.5	92.3
	NIR	96.9	-	-	97.4	96.6

Fe_2O_3 is frequently used as a deep red pigment which leads to its low TSR and NIR reflectance of 24 and 31.9%. All the synthesized Fe_2O_3-TiO_2 provided TSR and NIR reflectance higher than Fe_2O_3 where the reflectance was enhanced by around 20 to 50%. The highest reflectance belonged to Fe104 which has 67.8 and 86.3% of TSR and NIR reflectance as listed in **Table 4.5**.

Table 4.5

TSR and NIR Reflectance of the Fe_2O_3-TiO_2 Synthesized With Different Conditions Compared to Pure TiO_2 and Fe_2O_3

Reflectance (%R)						
TTIP (ml)		Gelation Time (hours)				
			3		6	10
		RT	40°C	60°C	RT	RT
Fe_2O_3	TSR	24	-	-	-	-
	NIR	31.9	-	-	-	-
TiO_2	TSR	98.2	-	-	-	-
	NIR	100.3	-	-	-	-
3	TSR	41.4	45.5	41.3	65.1	66.8
	NIR	69.3	67.6	60.6	83.8	85.5
4	TSR	46.2	-	-	60.6	67.8
	NIR	67.8	-	-	80.6	86.3
5	TSR	47.7	-	-	66.0	67.6
	NIR	69.9	-	-	84.6	85.2

The deep green color of Cr_2O_3 offers low TSR and NIR reflectivity of 40.1 and 59.8% and improved after coating with TiO_2 shell as listed in **Table 4.6**. The reflectance was improved by around 4 to 35% and the highest value belonged to Cr065 with 75 and 88.6% of TSR and NIR reflectance, respectively.

Table 4.6

TSR and NIR Reflectance of the Cr_2O_3-TiO_2 Synthesized With Different Conditions Compared to Pure TiO_2 and Cr_2O_3

Reflectance (%R)						
TTIP (ml)		Gelation Time (hours)				
			3		6	10
		RT	40°C	60°C	RT	RT
Cr_2O_3	TSR	40.1	-	-	-	-
	NIR	59.8	-	-	-	-
TiO_2	TSR	98.2	-	-	-	-
	NIR	100.3	-	-	-	-
3	TSR	44.2	46.2	39.4	75.2	72.2
	NIR	64.0	65.3	57.5	86.6	85.6
4	TSR	45.7	-	-	74.5	68.7
	NIR	65.1	-	-	88.0	84.8
5	TSR	62.0	-	-	75.0	57.1
	NIR	78.0	-	-	88.6	75.4

In addition, different metal oxides provided different trends as summarized in **Table 4.7**. For Al_2O_3-TiO_2 core-shell particles, NIR reflectance increased as TTIP volume increased when the gelation time was fixed at 10 hours. Al_2O_3 reflectance spectrum drops after around 1350 nm which is in the range of the NIR region. Meanwhile, the synthesized particles provide higher reflectance with characteristic peaks of TiO_2 around 1450 and 1940 nm.

For Fe_2O_3-TiO_2 core-shell particles, NIR reflectance decreased as the gelation temperature increased when TTIP volume was fixed at 3 ml. Another trend on Fe_2O_3-TiO_2 particles was the increase of NIR reflectance as the gelation time increased when the TTIP volume was fixed at 3, 4, and 5 ml. The reflectance of Fe_2O_3 increased after 550 nm which provided red color and its characteristic peaks are at 750 and 1050 nm (Saha & Bhunia, 2013). While the addition of TiO_2 shell provided higher reflectance in the NIR region similar to Al_2O_3-TiO_2.

In the case of Cr_2O_3-TiO_2 core-shell particles, NIR reflectance increased as the TTIP volume increased when the gelation time was fixed at 3 and 6 hours. Another trend of Cr_2O_3-TiO_2 is the decrease of NIR reflectivity as the TTIP volume increased at 10 hours of gelation. The characteristic peak of Cr_2O_3 around 420 and 540 nm provided green color (Tsegay et al., 2021).

The overall result showed that the addition of TiO_2 shell provided higher NIR reflectivity to the metal oxide cores. However, the effect of TTIP volume, gelation time, and gelation temperature must be further repeated and studied (see Appendix for NIR reflectance spectra).

Table 4.7

The Table Summarizes the Trends From TSR and NIR Reflectance

Increasing of	Fixed parameter	Al_2O_3-TiO_2	Fe_2O_3-TiO_2	Cr_2O_3-TiO_2
Gelation Temperature	3ml TTIP	-	↓	-
TTIP Volume	3h gelation	-	-	↑
	6h gelation	-		↑
	10h gelation	↑		↓
Gelation Time	3ml TTIP	-	↑	-
	4ml TTIP			
	5ml TTIP			

4.5.2 Coating Samples

The synthesized pigments which have the highest NIR reflectance of each metal oxide core were selected and coated on aluminum substrates for further cooling effect evaluation. The selected Al033, Fe104, Cr065, and their coatings were shown in **Figure 4.17 (a., b., and c.)**. The coated samples also underwent reflectance characterization to observe TSR and NIR reflectivity compared to their references of metal oxide cores, TiO_2, white exterior paint, and aluminum substrate. The coatings were shown in **Figure 4.17 (d., e., f., g., h., i., j., k., and l.)**.

Figure 4.17

The Powder Samples Al033 (a.), Fe104 (b.), and Cr065(c.). The Coating of Al033 (d.), Fe104 (e.), Cr065 (f.), Al_2O_3 (g.), Fe_2O_3 (h.), Cr_2O_3 (i.), Exterior Paint (j.), and TiO_2 (k.). Aluminum Substrate (l.)

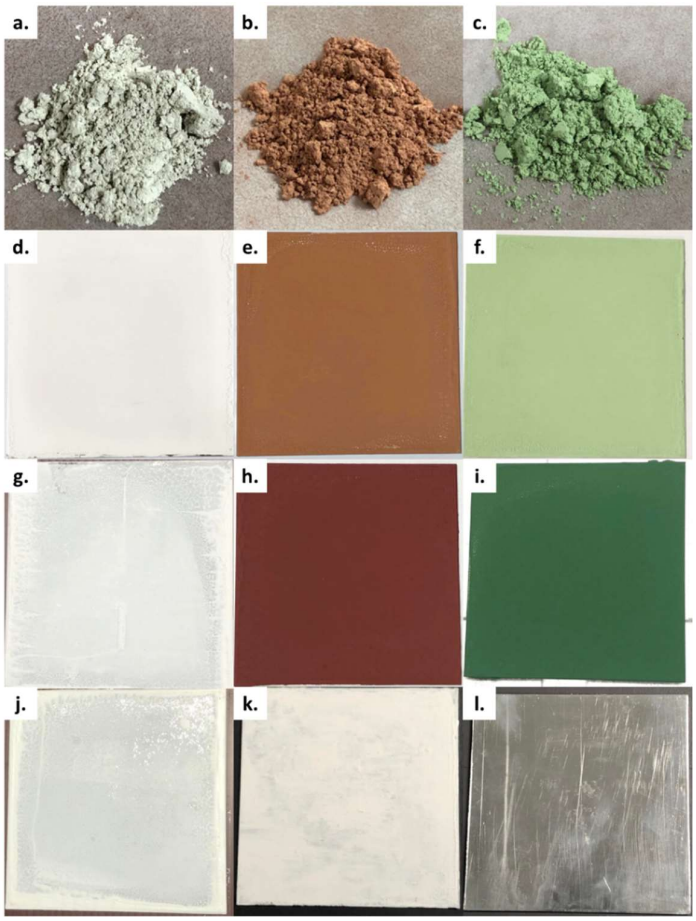

The TSR and NIR reflectance of the coatings were characterized as shown in percentage reflectance, **Table 4.8**, and reflectance spectra in **Figure 4.18**. The reflectivity of the aluminum substrate was high due to its natural shiny surface and low emissivity (FLUKE). Both paint and TiO_2 coatings also had high TSR and NIR reflectance from the property of TiO_2. Al033, Fe104, and Cr065 provided higher reflectance compared to the metal oxides alone which showed a potential to be NIR reflective pigments. Al033 improved the NIR reflectance from Al_2O_3 by 6.3%. Fe104 enhanced NIR

reflectance by 24.9% from the Fe_2O_3. Similarly, Cr065 improved the NIR reflectance from Cr_2O_3 by 20.4%.

Table 4.8

TSR and NIR Reflectance (%R) of the Coatings

Reflectance (%R)		
Coating	TSR	NIR
Aluminum substrate	81	90.1
Paint	70.8	70.5
TiO_2	85.7	84.5
Al_2O_3	79.1	77.8
Al033	82.1	84.1
Fe_2O_3	24.6	32.9
Fe104	44.8	57.8
Cr_2O_3	38.3	55.3
Cr065	62.5	75.7

Figure 4.18

Reflectance Spectra of the Coatings

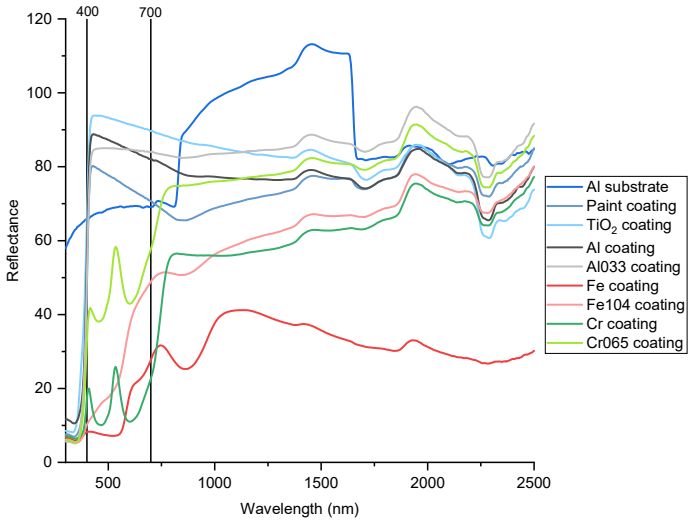

4.6 Cooling Effect Evaluation

To evaluate the cooling effect property further than the NIR reflectance characterization, the coatings underwent the cooling effect evaluation under the NIR light source. The temperature on the surface of the coatings was recorded with both thermocouples and a thermal camera as shown in **Figure 4.19 (a. and b.)**.

However, the temperature obtained from the thermal camera was higher than the value from thermocouples which might come from the different working principles. The thermal camera also has a limitation of low accuracy in the measurement of the low emissivity surface (FLUKE, 2015). As listed in **Table 4.9**, the absolute temperature from both thermal camera and thermocouples were comparable which supported the recorded temperature was reliable.

For the temperature on and under the substrate, the temperature was saturated after around 20 minutes. However, the temperature inside the box kept increasing from the heat transferring through the coated substrate and being insulated inside the box as shown in **Figure 4.19 (d.)**. The saturated temperatures of Al033, Fe104, and Cr065 were lower than the metal oxide cores as summarized in **Table 4.9**. Al033 reduced the

surface temperature and the temperature under the substrate by 2.9°C compared to the Al_2O_3 coating. Fe104 reduced the surface temperature and the temperature under the substrate from the Fe_2O_3 coatings by 7.98 and 6.73°C. Lastly, Cr065 reduced 6.42 and 5.90°C on and under the substrate's temperature from Cr_2O_3. Consequently, the amount of reduced temperature corresponded to the difference in percent reflectance between metal oxides and synthesized samples.

Figure 4.19

The Temperature on the Coatings Captured via Thermal Camera (a.) and Thermocouples (B.), the Temperature Under the Substrates (C.), and the Temperature Inside the Box (D.)

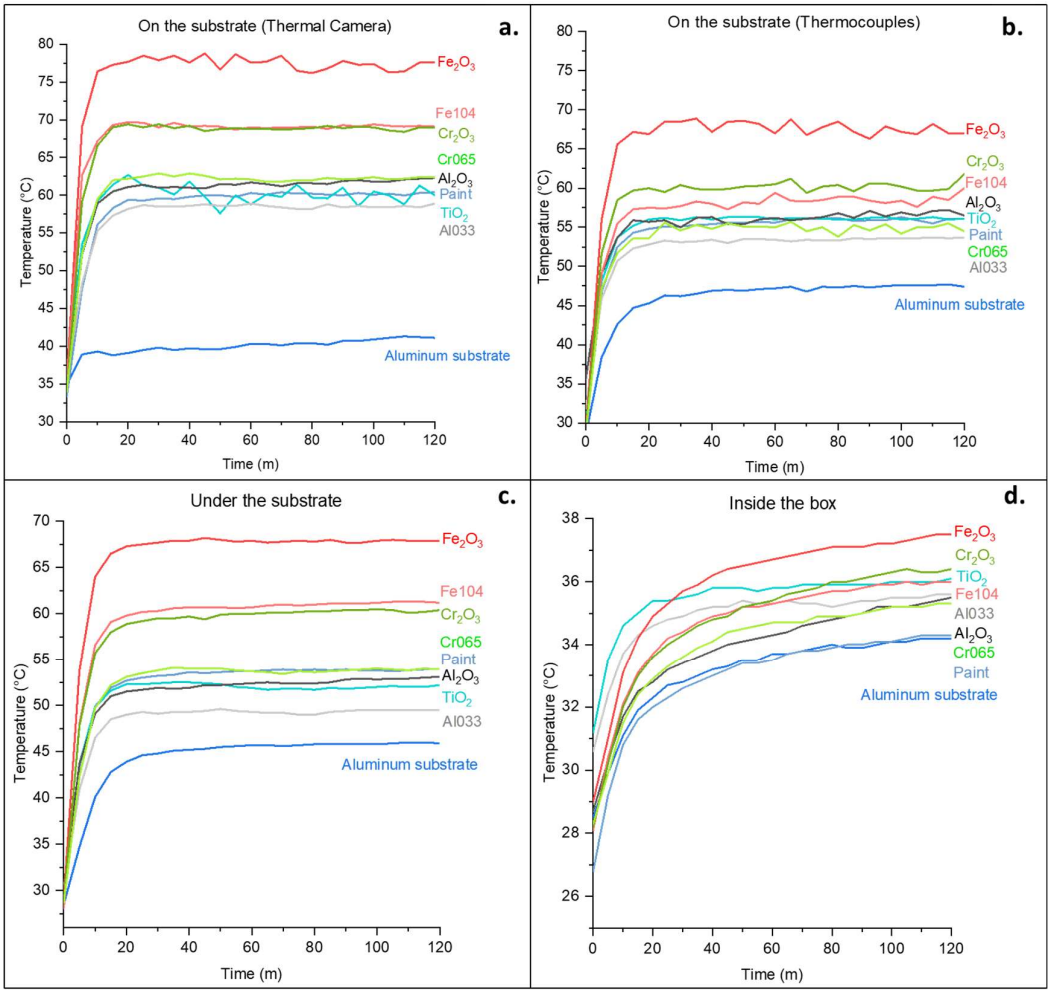

Table 4.9

Absolute Temperature Captured via a Thermal Camera and Thermocouples and the Temperature Difference Between the Temperature on the Surface and Under the Substrate of Metal Oxide Coatings and the Synthesized Particles

Coatings	Thermal camera		Thermometer		ΔT Under the substrate metal oxide-synthesized (°C)
	Absolute Temperature: T_{max}-T_{min} (°C)	ΔT On the surface: metal oxide-synthesized (°C)	Absolute Temperature: T_{max}-T_{min} (°C)	ΔT On the surface: metal oxide-synthesized (°C)	
Aluminum substrate	6.4	-	19.2	-	-
Paint	27.0	-	27.3	-	-
TiO_2	26.0	-	26.2	-	-
Al_2O_3	27.8	-	21.5	-	-
Al033	23.2	2.91	21.9	2.94	2.91
Fe_2O_3	43.2	-	39.9	-	-
Fe104	34.2	7.98	31.9	9.00	6.73
Cr_2O_3	35.4	-	33.0	-	-
Cr065	28.9	6.42	27.0	5.13	5.90

CHAPTER 5
CONCLUSION & RECOMMENDATIONS

5.1 Conclusion

The core-shell nanoparticles of Al_2O_3-TiO_2, Fe_2O_3-TiO_2, and Cr_2O_3-TiO_2 were successfully fabricated via a simple sol-gel synthesis as confirmed with SEM-EDS, TEM-EDS-SAED, and XRD. However, some parts of the samples could be the mixing of metal oxides and anatase TiO_2 and some could be the core-shell structure. In terms of optimization conditions, a gelation time of 6 hours was enough to complete the gelation of the TiO_2 shell and the temperature at RT was practical.

The synthesized pigments then underwent TSR and NIR reflectance characterization to identify their reflectivity. Al033 enhanced the NIR reflectance from the Al_2O_3 by 1.7%. Fe104 improved the NIR reflectance from Fe_2O_3 up to 54.4%. Lastly, Cr065 provided 28.8% higher NIR reflectance than Cr_2O_3. After coated on the aluminum substrate, Al033, Fe104, and Cr065 offered 6.3, 24.9, and 20.4% NIR reflectance higher than the coated metal oxides with the same percent weight in external commercial paint.

Moreover, to mimic the application of the pigments, the coatings underwent indoor cooling effect evaluation under the NIR irradiation. Compared to the metal oxides coatings, Al033, Fe104, and Cr065 provided 2.94, 9, and 5.13°C lower surface temperature which revealed the cooling effect of the synthesized pigments corresponding to their percent reflectance.

5.2 Recommendation

The complete gelation time of the TiO_2 could be in between 3 to 6 hours and identifying the exact time could reduce the total synthesis time. The effect of the increase of the gelation time and TTIP volume on the improvement of NIR reflectivity could be also further studied to find the optimum condition of synthesis for each metal oxide.

In this study, tween 80 was utilized as the surfactant and the amount of tween 80 might affect the formation of TiO_2 shell as well. Therefore, the surfactant chemical and amount of surfactant could be further improved.

For the cooling effect evaluation, the thermal camera might not be appropriate for continuous monitoring since the camera's temperature increased rapidly after a few minutes which could be unhealthy for the battery.

REFERENCES

Akbari, H. (2005). Energy Saving Potentials and Air Quality Benefits of Urban Heat IslandMitigation.

Akbari, H., Kurn, D. M., Bretz, S. E., & Hanford, J. W. (1997). Peak power and cooling energy savings of shade trees. *Energy and buildings, 25*(2), 139-148.

Ashraf, M. A., Peng, W., Zare, Y., & Rhee, K. Y. (2018). Effects of size and aggregation/agglomeration of nanoparticles on the interfacial/interphase properties and tensile strength of polymer nanocomposites. *Nanoscale research letters, 13*(1), 1-7.

Athar, T. (2015). Smart precursors for smart nanoparticles. In *Emerging Nanotechnologies for Manufacturing* (pp. 444-538). Elsevier.

Biagini, P., Thèves, C., Balaresque, P., Geraut, A., Cannet, C., Keyser, C., Nikolaeva, D., Gerard, P., Duchesne, S., & Orlando, L. (2012). Variola virus in a 300-year-old Siberian mummy. *New England journal of medicine, 367*(21), 2057-2059.

Busabok, C., Khongwong, W., Somwongsa, P., Ngernchuklin, P., Saensing, A., & Kanchanasutha, S. (2018). Preparation of Near-Infrared (NIR) Reflective Pigment by Solid State Reaction between Fe2O3 and Al2O3. Key Engineering Materials,

Caminade, C., McIntyre, K. M., & Jones, A. E. (2019). Impact of recent and future climate change on vector-borne diseases. *Annals of the New York Academy of Sciences, 1436*(1), 157.

Castells-Quintana, D., del Pilar Lopez-Uribe, M., & McDermott, T. K. (2018). Adaptation to climate change: A review through a development economics lens. *World Development, 104*, 183-196.

CDC. (2019, September 13, 2019). *Key Facts About Influenza (Flu)*. Retrieved June 11 from https://www.cdc.gov/flu/about/keyfacts.htm

CDC. (2021, Febuary 20, 2021). *History of Smallpox*. Retrieved 11 6 from https://www.cdc.gov/smallpox/history/history.html

CHEN, F.-X., FAN, W.-Q., ZHOU, T.-Y., & HUANG, W.-H. (2013). Core-Shell Nanospheres (HP-Fe2O3@ TiO2) with Hierarchical Porous Structures and Photocatalytic Properties. *Acta Physico-Chimica Sinica, 29*(1), 167-175.

Chen, J., Xie, W., Guo, X., Huang, B., Xiao, Y., & Sun, X. (2020). Near infrared reflective pigments based on Bi3YO6 for heat insulation. *Ceramics International, 46*(15), 24575-24584.

Degirmenci, K., Desouza, K. C., Fieuw, W., Watson, R. T., & Yigitcanlar, T. (2021). Understanding policy and technology responses in mitigating urban heat islands: A literature review and directions for future research. *Sustainable cities and society*, 102873.

Deilami, K., & Kamruzzaman, M. (2017). Modelling the urban heat island effect of smart growth policy scenarios in Brisbane. *Land Use Policy, 64*, 38-55.

Doebelin, N., & Kleeberg, R. (2015). Profex: a graphical user interface for the Rietveld refinement program BGMN. *Journal of applied crystallography, 48*(5), 1573-1580.

Du, H., Wang, D., Wang, Y., Zhao, X., Qin, F., Jiang, H., & Cai, Y. (2016). Influences of land cover types, meteorological conditions, anthropogenic heat and urban area on surface urban heat island in the Yangtze River Delta Urban Agglomeration. *Science of the Total Environment, 571*, 461-470.

EERE. *Energy Efficiency vs. Energy Intensity*. Retrieved 17 June from https://www.energy.gov/eere/analysis/energy-efficiency-vs-energy-intensity

EPA. *Climate Change Indicators: U.S. and Global Temperature* https://www.epa.gov/climate-indicators/climate-change-indicators-us-and-global-temperature

FLUKE. *Emissivity - Metals*. Retrieved 15 July from https://www.flukeprocessinstruments.com/en-us/service-and-support/knowledge-center/infrared-technology/emissivity-metals

FLUKE. (2015). *FLUKE Tis10 User Manual*

Fouillet, A., Rey, G., Laurent, F., Pavillon, G., Bellec, S., Guihenneuc-Jouyaux, C., Clavel, J., Jougla, E., & Hémon, D. (2006). Excess mortality related to the August 2003 heat wave in France. *International archives of occupational and environmental health, 80*(1), 16-24.

Fouque, F., & Reeder, J. C. (2019). Impact of past and on-going changes on climate and weather on vector-borne diseases transmission: a look at the evidence. *Infectious diseases of poverty, 8*(1), 1-9.

Gago, E. J., Roldan, J., Pacheco-Torres, R., & Ordóñez, J. (2013). The city and urban heat islands: A review of strategies to mitigate adverse effects. *Renewable and Sustainable Energy Reviews, 25*, 749-758. https://doi.org/https://doi.org/10.1016/j.rser.2013.05.057

Giridharan, R., & Emmanuel, R. (2018). The impact of urban compactness, comfort strategies and energy consumption on tropical urban heat island intensity: A review. *Sustainable cities and society, 40*, 677-687.

Guo, G., Wu, Z., Xiao, R., Chen, Y., Liu, X., & Zhang, X. (2015). Impacts of urban biophysical composition on land surface temperature in urban heat island clusters. *Landscape and Urban Planning, 135*, 1-10.

Hallegatte, S., & Rozenberg, J. (2017). Climate change through a poverty lens. *Nature Climate Change, 7*(4), 250-256.

He, X., Wang, F., Liu, H., Li, J., & Niu, L. (2017). Fabrication of highly dispersed NiTiO3@ TiO2 yellow pigments with enhanced NIR reflectance. *Materials Letters, 208*, 82-85.

Huang, B., Xiao, Y., Huang, C., Chen, J., & Sun, X. (2017). Environment-friendly pigments based on praseodymium and terbium doped La2Ce2O7 with high near-infrared reflectance: synthesis and characterization. *Dyes and Pigments, 147*, 225-233.

Huang, Y.-W., Cambre, M., & Lee, H.-J. (2017). The toxicity of nanoparticles depends on multiple molecular and physicochemical mechanisms. *International journal of molecular sciences, 18*(12), 2702.

Ianoș, R., Muntean, E., Băbuță, R., Lazău, R., Păcurariu, C., & Bandas, C. (2017). Combustion synthesis of pink chromium-doped alumina with excellent near-infrared reflective properties. *Ceramics International, 43*(2), 2568-2572.

Ianoş, R., Muntean, E., Lazău, R., Băbuță, R., Moacă, E.-A., Păcurariu, C., Dabici, A., & Hulka, I. (2018). One-step synthesis of near-infrared reflective brown pigments based on iron-doped lanthanum aluminate, LaAl1-xFexO3. *Dyes and Pigments, 152*, 105-111.

Ianoş, R., Muntean, E., Păcurariu, C., Lazău, R., Bandas, C., & Delinescu, G. (2017). Combustion synthesis of a blue Co-doped zinc aluminate near-infrared reflective pigment. *Dyes and Pigments, 142*, 24-31.

Isaac, M., & Van Vuuren, D. P. (2009). Modeling global residential sector energy demand for heating and air conditioning in the context of climate change. *Energy policy, 37*(2), 507-521.

Jamei, E., Rajagopalan, P., Seyedmahmoudian, M., & Jamei, Y. (2016). Review on the impact of urban geometry and pedestrian level greening on outdoor thermal comfort. *Renewable and Sustainable Energy Reviews, 54*, 1002-1017. https://doi.org/https://doi.org/10.1016/j.rser.2015.10.104

Jose, S., Joshy, D., Narendranath, S. B., & Periyat, P. (2019). Recent advances in infrared reflective inorganic pigments. *Solar Energy Materials and Solar Cells, 194*, 7-27.

Karunakaran, C., Magesan, P., Gomathisankar, P., & Vinayagamoorthy, P. (2015). Absorption, emission, charge transfer resistance and photocatalytic activity of Al2O3/TiO2 core/shell nanoparticles. *Superlattices and Microstructures, 83*, 659-667. https://doi.org/https://doi.org/10.1016/j.spmi.2015.04.014

Kim, S.-E., Woo, J.-Y., Kang, S.-Y., Min, B. K., Lee, J. K., & Lee, S.-W. (2016). A facile general route for ternary Fe2O3@ TiO2@ nanometal (Au, Ag) composite as a high-performance and recyclable photocatalyst. *Journal of Industrial and Engineering Chemistry, 43*, 142-149. https://doi.org/https://doi.org/10.1016/j.jiec.2016.07.060

Kolokotroni, M., Giannitsaris, I., & Watkins, R. (2006). The effect of the London urban heat island on building summer cooling demand and night ventilation strategies. *Solar energy, 80*(4), 383-392.

Lan, L., Wargocki, P., Wyon, D. P., & Lian, Z. (2011). Effects of thermal discomfort in an office on perceived air quality, SBS symptoms, physiological responses, and human performance. *Indoor air, 21*(5), 376-390.

Legendre, M., Bartoli, J., Shmakova, L., Jeudy, S., Labadie, K., Adrait, A., Lescot, M., Poirot, O., Bertaux, L., & Bruley, C. (2014). Thirty-thousand-year-old distant relative of giant icosahedral DNA viruses with a pandoravirus morphology. *Proceedings of the National Academy of Sciences, 111*(11), 4274-4279.

Li, M., Gu, S., Bi, P., Yang, J., & Liu, Q. (2015). Heat waves and morbidity: current knowledge and further direction-a comprehensive literature review. *International journal of environmental research and public health, 12*(5), 5256-5283.

Lipczynska, A., Schiavon, S., & Graham, L. T. (2018). Thermal comfort and self-reported productivity in an office with ceiling fans in the tropics. *Building and Environment, 135*, 202-212.

Llana, M., Tolentino, M., Valeza, N., Reyes, J., & Basilia, B. (2021). Release Analysis of Nano-Titanium Dioxide (TiO2) from Paint: An Accelerated Weathering Experiment. IOP Conference Series: Materials Science and Engineering,

Lundgren, K., & Kjellstrom, T. (2013). Sustainability challenges from climate change and air conditioning use in urban areas. *Sustainability, 5*(7), 3116-3128.

Malshe, V. C., & Bendiganavale, A. K. (2008). Infrared reflective inorganic pigments. *Recent Patents on Chemical Engineering, 1*(1), 67-79.

Manning, C., & Clayton, S. (2018). Threats to mental health and wellbeing associated with climate change. In *Psychology and climate change* (pp. 217-244). Elsevier.

Manso, M., Teotónio, I., Silva, C. M., & Cruz, C. O. (2021). Green roof and green wall benefits and costs: A review of the quantitative evidence. *Renewable and Sustainable Energy Reviews, 135*, 110111.

Marotzke, J., Semmann, D., & Milinski, M. (2020). The economic interaction between climate change mitigation, climate migration and poverty. *Nature Climate Change, 10*(6), 518-525.

Meenakshi, P., & Selvaraj, M. (2018). Bismuth titanate as an infrared reflective pigment for cool roof coating. *Solar Energy Materials and Solar Cells, 174*, 530-537.

Morton, J. F. (2007). The impact of climate change on smallholder and subsistence agriculture. *Proceedings of the National Academy of Sciences, 104*(50), 19680-19685.

Müller, R., Reuss, F., Kendrovski, V., & Montag, D. (2019). Vector-borne diseases. *Biodiversity and Health in the Face of Climate Change, 481*.

Nordhaus, W. (2019). Climate change: the ultimate challenge for economics. *American Economic Review, 109*(6), 1991-2014.

Peterson, D. L., & Halofsky, J. E. (2018). Adapting to the effects of climate change on natural resources in the Blue Mountains, USA. *Climate Services, 10*, 63-71.

Qi, Y., Xiang, B., & Zhang, J. (2017). Effect of titanium dioxide (TiO2) with different crystal forms and surface modifications on cooling property and surface wettability of cool roofing materials. *Solar Energy Materials and Solar Cells, 172*, 34-43.

RICC, M., Razio, B., Poletti, L., Panato, C., Balzarini, F., Mezzoiuso, A., & Vezzosi, L. (2020). Risk perception of heat related disorders on the workplaces: a survey among health and safety representatives from the autonomous province of Trento, Northeastern Italy. *Journal of preventive medicine and hygiene, 61*(1), E48.

Ritchie, H., & Roser, M. (2017). Fossil fuels. *Our world in data*. https://ourworldindata.org/fossil-fuels

Rosati, A., Fedel, M., & Rossi, S. (2021). NIR reflective pigments for cool roof applications: A comprehensive review. *Journal of Cleaner Production*, 127826.

Roser, H. R. a. M. (2020). *Energy* https://ourworldindata.org/energy

Sadeghi-Niaraki, S., Ghasemi, B., Habibolahzadeh, A., Ghasemi, E., & Ghahari, M. (2019). Nanostructured Fe2O3@ TiO2 pigments with improved NIR reflectance and photocatalytic ability. *Materials Chemistry and Physics, 235*, 121769.

Saha, S., & Bhunia, A. (2013). Synthesis of Fe2O3 nanoparticles and study of its structural, optical properties.

Santamouris, M. (2014). Cooling the cities–a review of reflective and green roof mitigation technologies to fight heat island and improve comfort in urban environments. *Solar energy, 103*, 682-703. https://doi.org/https://doi.org/10.1016/j.solener.2012.07.003

Scott, D., Hall, C. M., & Gössling, S. (2019). Global tourism vulnerability to climate change. *Annals of Tourism Research, 77*, 49-61.

Semenza, J. C., Rubin, C. H., Falter, K. H., Selanikio, J. D., Flanders, W. D., Howe, H. L., & Wilhelm, J. L. (1996). Heat-related deaths during the July 1995 heat wave in Chicago. *New England journal of medicine, 335*(2), 84-90.

Shafique, M., Kim, R., & Rafiq, M. (2018). Green roof benefits, opportunities and challenges–A review. *Renewable and Sustainable Energy Reviews, 90*, 757-773.

Shah, K. W., Huseien, G. F., & Kua, H. W. (2021). A state-of-the-art review on core–shell pigments nanostructure preparation and test methods. Micro,

Sharma, R., Tiwari, S., & Tiwari, S. K. (2018). Highly reflective nanostructured titania shell: a sustainable pigment for cool coatings. *ACS Sustainable Chemistry & Engineering, 6*(2), 2004-2010.

Tan, J. Z., Xia, F., & Maroto-Valer, M. M. (2019). Raspberry-Like Microspheres of Core–Shell Cr2O3@ TiO2 Nanoparticles for CO2 Photoreduction. *ChemSusChem, 12*(24), 5246.

Tauseef Hassan, S., Xia, E., & Lee, C.-C. (2021). Mitigation pathways impact of climate change and improving sustainable development: The roles of natural resources, income, and CO2 emission. *Energy & Environment, 32*(2), 338-363.

Thongkanluang, T., Limsuwan, P., & Rakkwamsuk, P. (2011). Preparation and Application of High Near-Infrared Reflective Green Pigment for Ceramic Tile Roofs. *International Journal of Applied Ceramic Technology, 8*(6), 1451-1458.

Tsegay, M., Gebretinsae, H., & Nuru, Z. (2021). Structural and optical properties of green synthesized Cr2O3 nanoparticles. *Materials Today: Proceedings, 36*, 587-590.

Tumpey, T. M., Basler, C. F., Aguilar, P. V., Zeng, H., Solórzano, A., Swayne, D. E., Cox, N. J., Katz, J. M., Taubenberger, J. K., & Palese, P. (2005). Characterization of the reconstructed 1918 Spanish influenza pandemic virus. *science, 310*(5745), 77-80.

WHO. (2020). *Vector-borne diseases*. Retrieved 10 6 2021 from https://www.who.int/en/news-room/fact-sheets/detail/vector-borne-diseases

Xiang, B., Qi, Y., Wang, S., & Zhang, J. (2015). Using a novel and easy-to-use sandwich structure device to evaluate the cooling properties of cool materials. *International Journal of Polymer Analysis and Characterization, 20*(6), 529-540.

Xu, Q.-T., Li, J.-C., Xue, H.-G., & Guo, S.-P. (2018). Binary iron sulfides as anode materials for rechargeable batteries: Crystal structures, syntheses, and electrochemical performance. *Journal of Power Sources, 379*, 41-52.

Yang, K., Yi, H., Tang, X., Zhao, S., Gao, F., Huang, Y., Yang, Z., Wang, J., Shi, Y., & Xie, X. (2019). Reducing the competitive adsorption between SO2 and NO by Al2O3@ TiO2 core-shell structure adsorbent. *Chemical Engineering Journal, 364*, 420-427.

You, Z., Zhang, M., Wang, J., Pei, W., & Li, G. (2021). Experimental study of optical and cooling performances of CuO and TiO2 near-infrared reflective blending coatings. *Solar energy, 225*, 19-32.

Zhang, J., Zhu, C., Lv, J., Zhang, W., & Feng, J. (2018). Preparation of colorful, infrared-reflective, and superhydrophobic polymer films with obvious resistance to dust deposition. *ACS applied materials & interfaces, 10*(46), 40219-40227.

Zhang, X., Xie, Y., Chen, H., Guo, J., Meng, A., & Li, C. (2014). One-dimensional mesoporous Fe2O3@ TiO2 core–shell nanocomposites: Rational design, synthesis and application as high-performance photocatalyst in visible and UV light region. *Applied surface science, 317*, 43-48.

APPENDIX

Figure A1 ***Graph Showing Trend of Increasing Reflectance Spectra as the TTIP Volume Increased for Samples Fabricated With 10 Hours of Gelation***

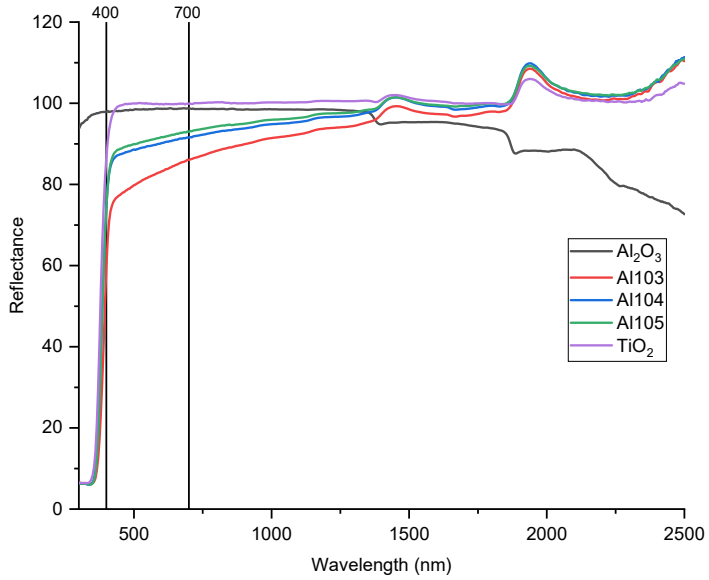

Figure A2 ***Graph Showing Trend of Decreasing Reflectance Spectra as the Gelation Temperature Increased for Samples Fabricated With 3ml TTIP***

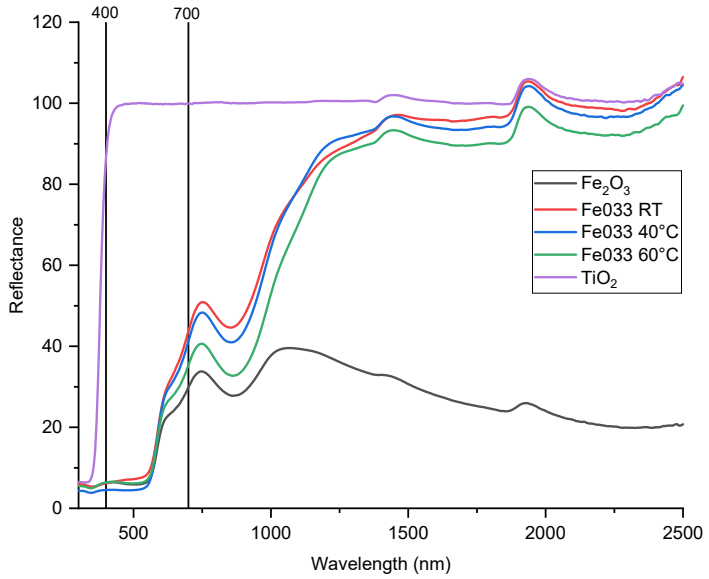

Figure A3 ***Graph Showing Trend of Increasing Reflectance Spectra as the Gelation Time Increased for Samples Fabricated With 3ml of TTIP***

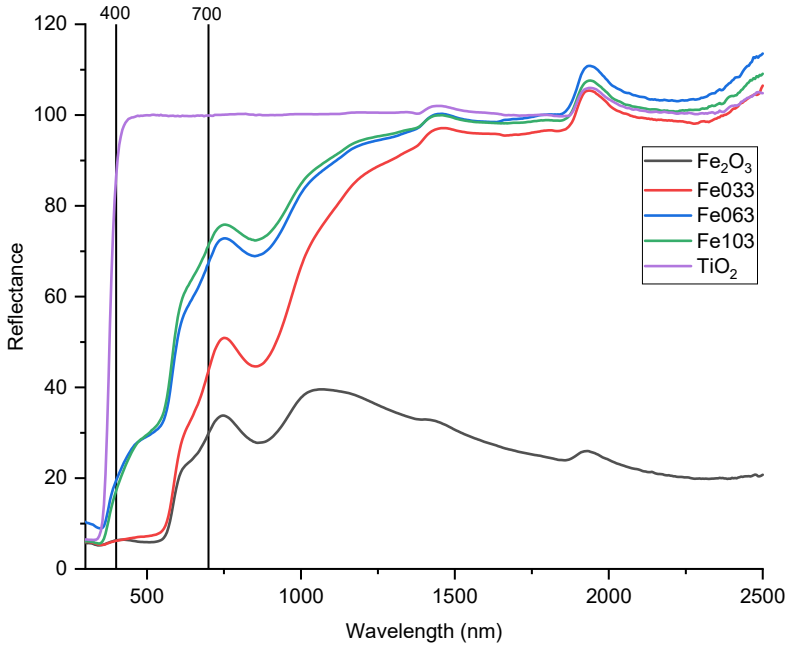

Figure A4 ***Graph Showing Trend of Increasing Reflectance Spectra as the Gelation Time Increased for Samples Fabricated With 4ml of TTIP***

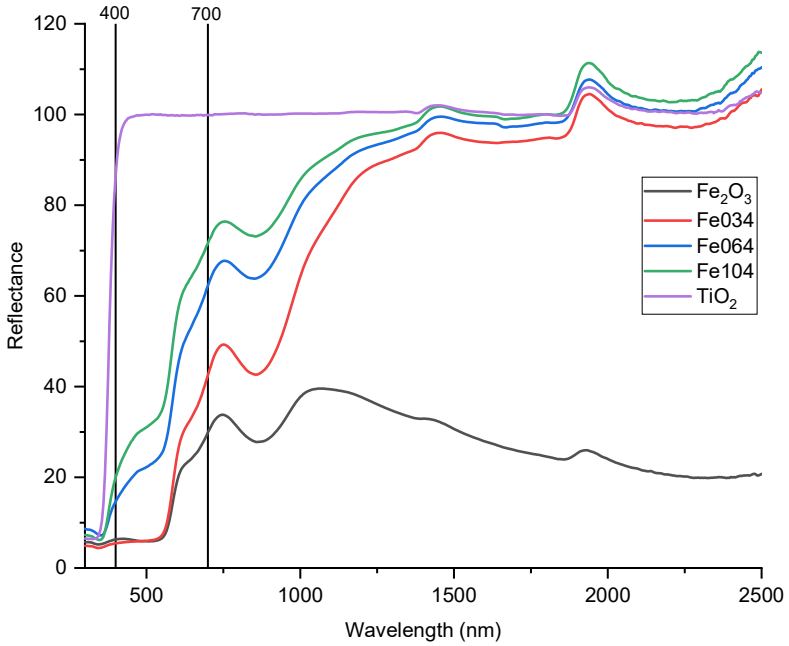

Figure A5 ***Graph Showing Trend of Increasing Reflectance Spectra as the Gelation Time Increased for Samples Fabricated With 5ml of TTIP***

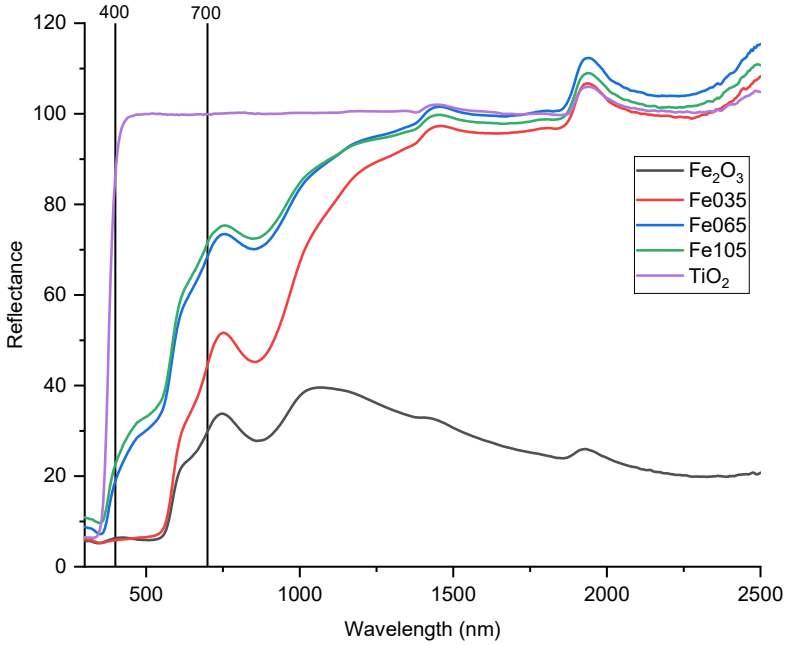

Figure A6 ***Graph Showing Trend of Increasing Reflectance Spectra as the TTIP Volume Increased for Samples Fabricated With 3 Hours of Gelation***

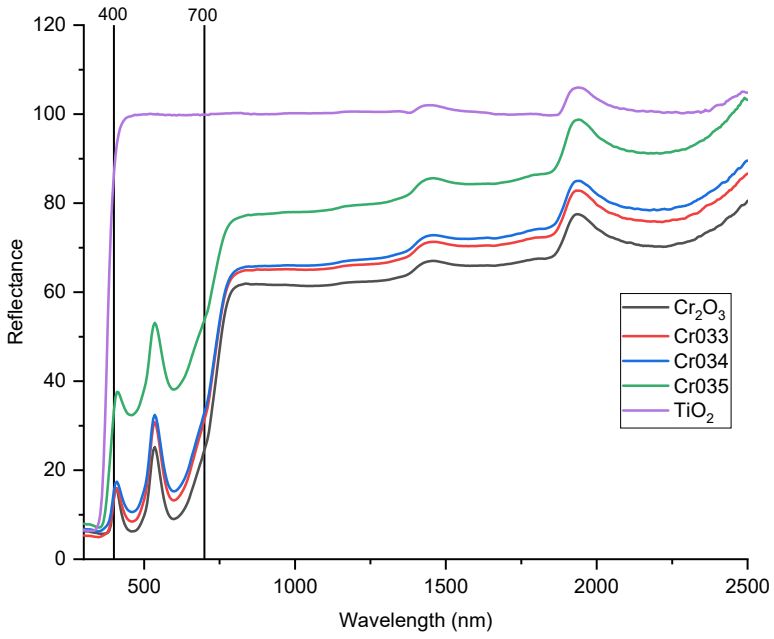

Figure A7 ***Graph Showing Trend of Increasing Reflectance Spectra as the TTIP Volume Increased for Samples Fabricated With 6 Hours of Gelation***

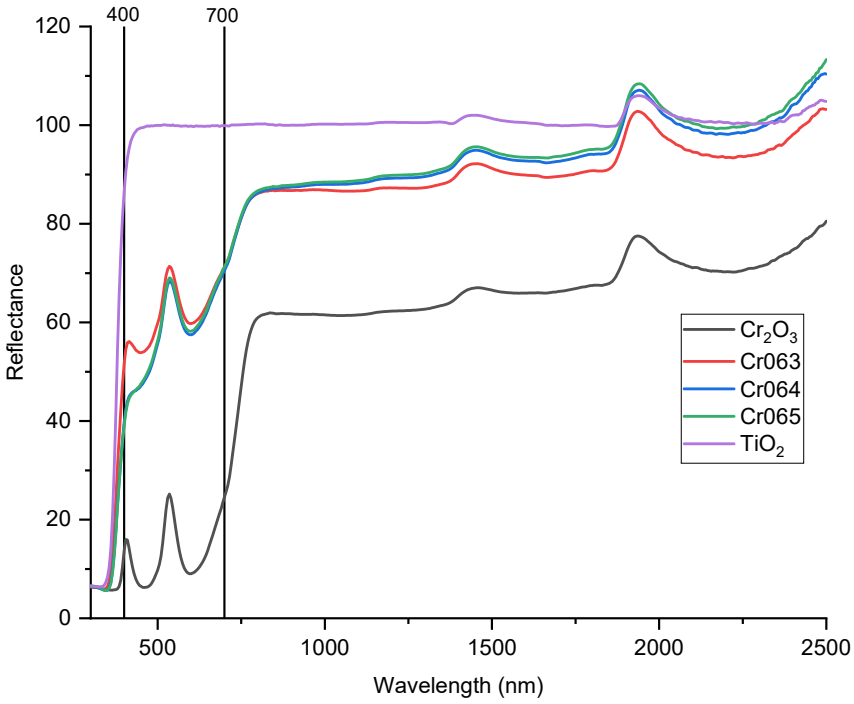

Figure A8 ***Graph Showing Trend of Decreasing Reflectance Spectra as the TTIP Volume Increased for Samples Fabricated With 3 Hours of Gelation***